Combined effects of urban planning and climate change on the climate of the Stuttgart Metropolitan Area

Kombinierte Auswirkungen von Bebauungsmaßnahmen und Klimawandel auf das Klima im Großraum Stuttgart

Masterarbeit im Fach Meteorologie
von

Hannah Imhof

Januar 2015

INSTITUT FÜR METEOROLOGIE UND KLIMAFORSCHUNG
KARLSRUHER INSTITUT FÜR TECHNOLOGIE (KIT)

Referent: Prof. Dr. Christoph Kottmeier
Koreferent: Prof. Dr. Corinna Hoose

Zusammenfassung

Ein wichtiger Aspekt heutiger Stadtplanung ist der Einfluss des Klimawandels auf das städtische Klima und somit das Wohlbefinden der Bewohner. Doch auch die Auswirkungen städtischer Planung auf das lokale Klima müssen berücksichtigt werden. Diese Arbeit zielt darauf ab, die kombinierten Effekte von Klimawandel und stadtplanerischen Maßnahmen herauszuarbeiten. Die Untersuchungen werden mit Hilfe von hochaufgelösten numerischen Klimasimulationen für den Großraum Stuttgart durchgeführt.

Das städtische Klima wird durch eine genauere Landnutzungsklassifizierung und den zusätzlich eingebauten anthropogenen Wärmeeintrag in dem Boden-Atmosphären-Modell Veg3D parametrisiert. Durch eine Koppelung an das regionale Klimamodell COSMO-CLM können die Auswirkungen städtischer Bebauung auf das lokale Klima des Großraums Stuttgart untersucht werden. Es wurden gekoppelte Simulationen mit einem horizontalen Gitterpunktsabstand von 0,025 ° (ca. 2,8 km) sowohl für einen Kontrollzeitraum (1971-1975) als auch einen Projektionszeitraum (2021-2025) durchgeführt. Um die Spannweite des Einflusses städtischer Bebauung auf das lokale Klima zu untersuchen, wurden zwei gegensätzliche stadtplanerische Szenarien erstellt. Das ‚grüne Szenario‘ nimmt eine Vergrößerung bepflanzter Flächen in bebauten Gebieten, sowie Aufforstung einer landwirtschaftlichen Fläche im Süden Stuttgarts und einen erniedrigten Ausstoß anthropogener Wärme an, das ‚rote Szenario‘ dagegen eine Zunahme und Verdichtung der bebauten Flächen. Zusätzlich wurde eine Projektion mit der gegenwärtigen Landnutzung des Kontrolllaufes durchgeführt, um den alleinigen Effekt des Klimawandels zu quantifizieren.

Für einen Test der erfolgreiche Implementierung der Änderungen an Veg3D wurden zunächst Stand-alone-Simulationen durchgeführt, bei denen das Bodenmodell von Atmosphärendaten eines vorherigen gekoppelten Laufes angetrieben wird, aber keinen Einfluss auf die Atmosphäre nehmen kann. Wie erwartet ergab sich eine mittlere Zunahme der Bodentemperatur von ca. 3 K in den obersten Schichten bei Berücksichtigung von anthropogener Wärme. Hierbei zeigte sich jedoch, dass die Temperaturzunahme in den unteren Schichten nach einem Jahr noch nicht auf einen konstanten Wert konvergiert ist, weshalb für den Referenzlauf ein zyklisches Einschwingen von Veg3D vorgenommen wurde. Dazu wurde Veg3D von den atmosphärischen Daten eines gekoppelten Laufes des ersten Simulationsjahres 1968 viermal hintereinander zyklisch angetrieben.

Außerdem wurden die Auswirkungen des grünen und roten Szenarios in Stand-alone-Simulationen getestet. Sie resultierten in einer mittleren Temperaturabnahme gegenüber

der Referenzsituation von ca. 2,5 K für das grüne, beziehungsweise einer Temperaturzunahme um ca. 1 K für das rote Szenario.

Die gekoppelten Simulationen ergaben für die Innenstadt von Stuttgart und die untersuchten Zeiträume eine signifikante Temperaturzunahme von 0,87 K. Im roten Szenario erhöhte sich diese um weitere 0,15 K, durch das grüne Szenario erniedrigte sich die Temperaturzunahme um 0,06 K. Signifikante, wenn auch kleine Änderungen durch den Klimawandel traten außerdem für Globalstrahlung, spezifische Feuchte und Gesamtbewölkung auf. Für die beiden Bebauungsszenarien waren diese in der Innenstadt jedoch weitaus kleiner.

Blickt man auf das gesamte Untersuchungsgebiet, das die Stadt Stuttgart und ihr näheres Umland einschließt, ergaben sich an einzelnen Gitterpunkten mit geänderter Landnutzung Differenzen, die im Bereich des Klimawandelsignals liegen. Hier war jedoch bereits das Klimawandelsignal relativ klein, was die Relevanz der Änderungen, die durch die Bebauungsszenarien hervorgerufen werden, schmälert. Ein Gitterpunkt, der im roten Szenario einen sehr hohen anthropogenen Wärmeinput von 300 W/m^2 aufweist, verursachte signifikante Änderungen der Temperatur und eine kleine lokale Konvektionszelle. Insgesamt ist der Einfluss des Klimawandels im Vergleich zum Einfluss der Bebauungsänderungen jedoch als größer zu bewerten.

Contents

1. Introduction

For a long time, aspects of urban climate did not affect urban planning, as stated and analysed, e.g., by Oke (1984). By now however, microclimate is considered in urban planning more often (e. g. Evans and de Schiller, 1996) and in Stuttgart, which is the city studied in this thesis, the special topographic situation has had an impact on urban planning for several decades (Scheef, 1976). It was already by the end of the 1930s that a meteorologist was employed to analyse the interrelation between urban climate and urban planning (Amt für Umweltschutz Stuttgart, 2013). The reason for the concern for urban climate in Stuttgart is its unique topography. It lies in a basin (so called *Kessellage*) which can cause poor air quality and increased temperatures (see section 3.1 for details).

An important issue of current urban planning is the impact of climate change on urban climate and whether mitigation measures are able to diminish this influence. In this thesis, the combined effects of different urban planning scenarios together with climate change on the Stuttgart Metropolitan Area (SMA) as well as the city centre of Stuttgart are analysed. The aim of this thesis is to decide, whether climate change or land use change has the larger impact on local climate in the SMA.

For that purpose, two opposite urban planning scenarios for the future have been developed. The 'green scenario' presumes an increase in vegetated surfaces and less energy consumption in urban areas as well as reforestation of an area south of Stuttgart, the 'red scenario' assumes an enlargement and densification of urban and industrial areas. These two scenarios span the possible impacts of urban development on future climate (Fig. 1.1 vertical). The time period for the projections is 2021-2025. To quantify the impact of climate change alone, one simulation for a control time period (1971-1975) and one projection with the reference land use have been conducted as well (Fig. 1.1 horizontal). Considering current emissions of greenhouse gases and climate policies, RCP 8.5 is the selected emission scenario. This scenario assumes continuously high greenhouse gas emissions (Moss et al., 2010).

For the analysis, high-resolution climate simulations with a horizontal grid spacing of 0.025 ° (approx. 2.8 km) have been performed by using the regional climate model (RCM) COSMO-CLM, coupled with the soil-vegetation-atmosphere-transfer (SVAT) model Veg3D. To better represent the different types of urban land use, more specific land use classes have been implemented in Veg3D. They are mostly based on the 'local climate

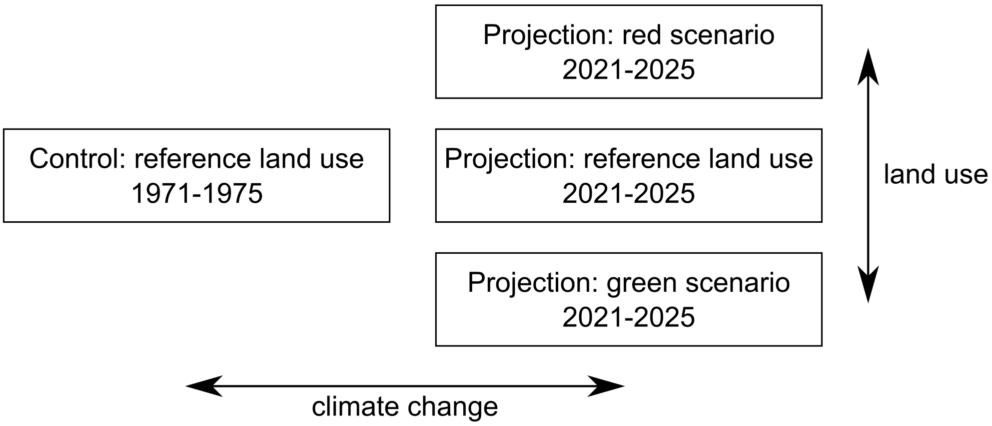

Figure 1.1: Concept of simulations

zones' (LCZ) by Stewart and Oke (2012). Additionally, anthropogenic heat input has been incorporated.

The advantage of conducting a modelling study rather than analysing observations is that one obtains a consistent set of many variables covering an entire domain. Additionally, any desired time period of climatic relevance can be analysed, and future climate can be estimated only by using model projections.

An overview of the state of urban climate science is given in the second chapter. It is followed by a chapter providing information on the climate and land use in Stuttgart including the two different scenarios for future urban land use. Chapter four describes the models used in this thesis and the changes that have been implemented to better represent urban areas. Several tests in a stand-alone mode of Veg3D are presented in chapter five. Thereafter, the final analysis of the coupled simulations is provided. The thesis concludes with a summary and an outlook.

2. Urban Climate

Climate in a city differs from that of its surrounding countryside. This chapter summarises the key features of urban climate that are relevant for this thesis. It also presents some studies of the effects of urban land use change that have been conducted before.

2.1 Urban Heat Island (UHI)

The term Urban Heat Island (UHI) describes the fact that the air temperature in a city is higher than in its surrounding countryside or suburbs (Fig. 2.1). At the transition of rural to urban areas, there is an abrupt increase in temperature ('cliff') followed by the 'plateau' with slightly increasing temperature but also colder spots at areas with large amounts of vegetation. Peak intensity of UHI (in literature often ΔT_{u-r}) is located in the city centre.
UHI is caused by a variety of mechanisms. One is enhanced absorption of short-wave radiation of the material used for buildings and streets. Additionally, this urban material has a high heat capacity causing less radiative emission during nights and thus an accumulation of heat.
Furthermore, there is a large amount of impervious surfaces in cities, fewer vegetation than in the countryside and rain water is quickly drained. This prevents the ground from

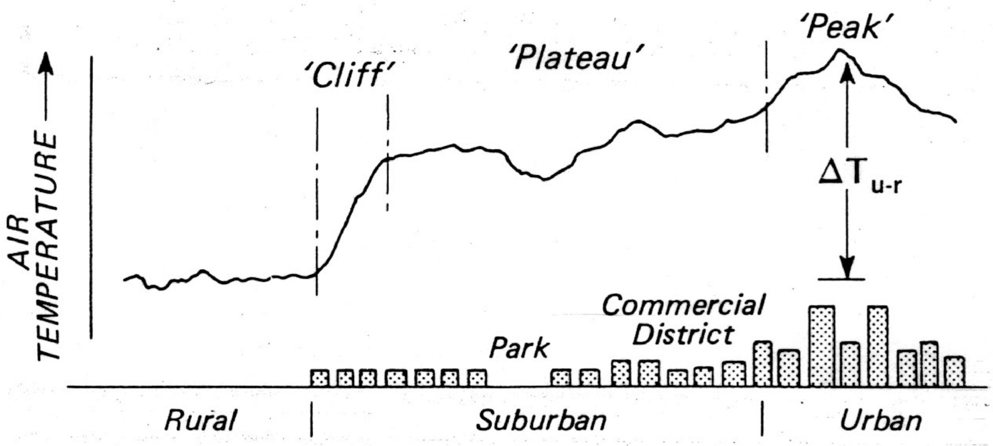

Figure 2.1: Spatial distribution of UHI (Oke, 1993)

buffering high temperatures through the consumption of latent heat by evapotranspiration (see, e.g. Carlson et al., 1981).

Also, the geometry of a city influences temperature: wind speed is reduced by high buildings resulting in fewer exchange of fresh and cool air (Oke, 1993). In street canyons, high buildings can trap radiation. Walls are being radiated differentially depending on their orientation and shading effects occur.

For short-wave radiation, more or less a balance between less radiation reaching the urban surface through air pollution by aerosols and gases and stronger absorption due to a lower albedo in urban areas exists. For long-wave radiation, it is believed that pollutants, especially aerosols, absorb and re-emit long-wave radiation resulting in a pseudo-greenhouse effect (Rizwan et al., 2008).

Anthropogenic heat release due to combustion, space heating or cooling, manufacturing, transport, etc. is an additional source for elevated temperature in a city (see, e.g. Oke, 1993). Section 2.2 will go into more detail on this topic.

UHI intensity depends on synoptic conditions. It is largest for cloudless and calm nights and exhibits a daily cycle (Fig. 2.2 a and c). Both the cooling rate after sunset and the heating rate after sunrise are larger and steeper for rural sites compared to urban areas due to the high heat capacity of urban material (Fig. 2.2 b). This results in the peak UHI

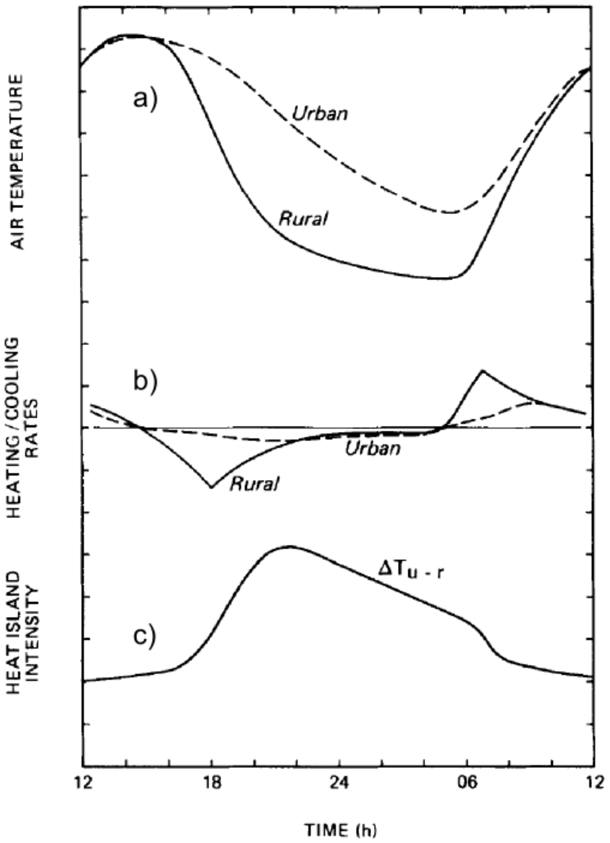

Figure 2.2: Idealised daily cycle of UHI (Oke, 1982)

intensity a few hours after sunset (Fig. 2.2 c). During the night, the urban cooling rate slightly exceeds the rural one until just after sunrise, when the rural heating rate again exceeds the urban one and UHI intensity approaches its minimum (Oke, 1982).
For Stuttgart, which is the city analysed in this thesis, UHI intensity can reach up to 7 ° C (Landeshauptstadt Stuttgart, 2008).
Apart from elevated surface temperatures, UHI can produce a so-called urban breeze (Fig. 2.3) similar to the sea breeze. The temperature gradient from rural to suburban to urban areas (Fig. 2.1) induces a horizontal pressure gradient. Thus, low level convergence evolves leading to colder air flow from the surrounding countryside and an updraft above the warm city centre. Divergence occurs in the upper boundary layer and the circulation is closed by slow downdrafts some distance away from the city (Hidalgo et al., 2010, 2008b).

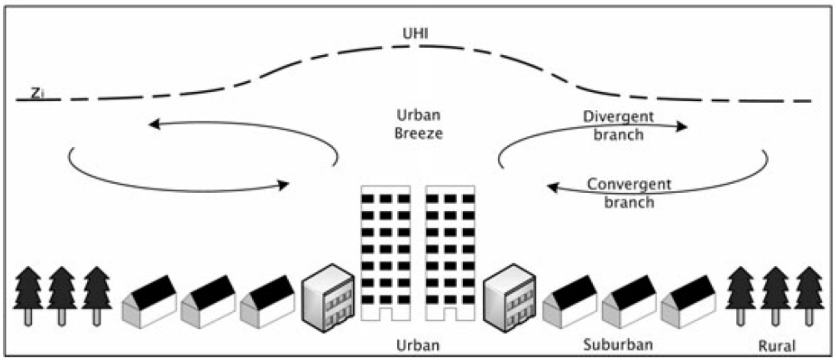

Figure 2.3: Urban breeze (Hidalgo et al., 2008a)

2.2 Anthropogenic Heat Input

As mentioned before, the release of additional heat by human activities like combustion, space heating or cooling, manufacturing and transport enhances the UHI effect. Thus, a model of urban climate has to include this additional heat source.
With anthropogenic heat release considered, Oke (1993) states the energy balance in an imaginary urban volume (Fig. 2.4) as follows:

$$Q^* + Q_F = Q_H + Q_E + \Delta Q_S + \Delta Q_A \tag{2.1}$$

where Q^*: net all-wave radiation flux density, positive if energy is gained
Q_F: anthropogenic heat flux density, $Q_F \geq 0$
Q_H: turbulent sensible heat flux density, positive for loss of heat
Q_E: turbulent latent heat flux density, positive for loss of heat
ΔQ_S: net energy storage, positive for storing of energy
ΔQ_A: net energy advection, positive for net advection of energy out of the volume

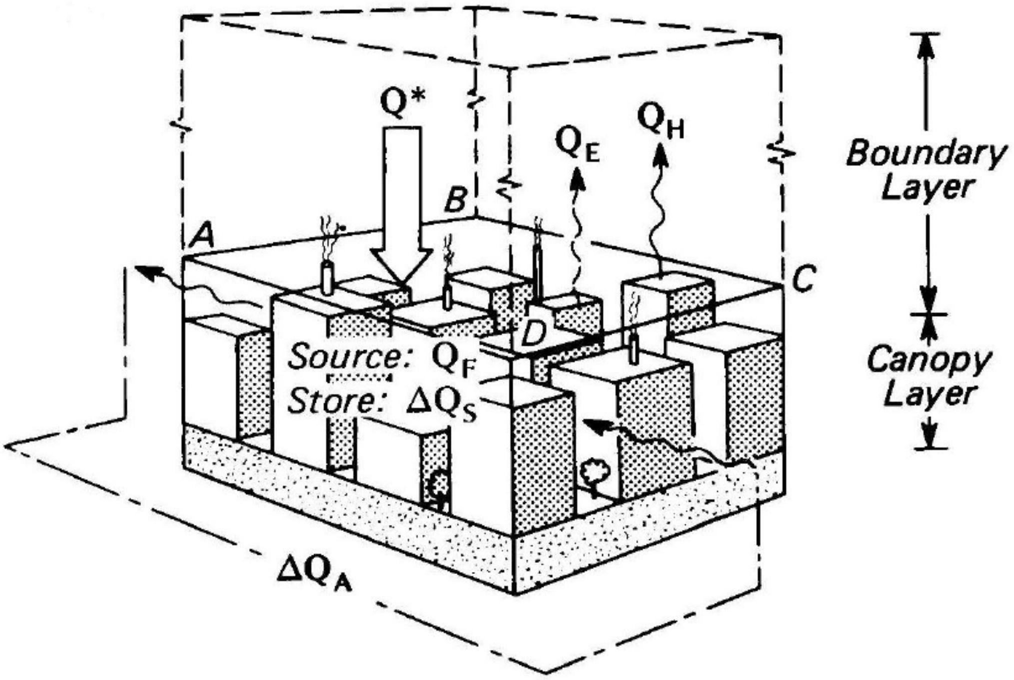

Figure 2.4: Energy fluxes in an imaginary urban volume (Oke, 1993) with positive directions of fluxes indicated as arrows

Q_F differs for different cities and also exhibits a pronounced annual cycle: Pigeon et al. (2007) state a Q_F for Toulouse (France) around 15 W/m^2 during summer and 70 W/m^2 during winter. On the other hand, Oke (1993) reports a summer Q_F for Manhattan (USA) of 53 W/m^2 and 265 W/m^2 during winter. The largest values of Q_F occur in cities at high latitudes during winter due to the additional heating load (Taha, 1997).
Oke (1982) found a relationship between the population of a city and its maximum heat island intensity $\Delta T_{u-r(max)}$ which is different for North America and Europe (Fig. 2.5).

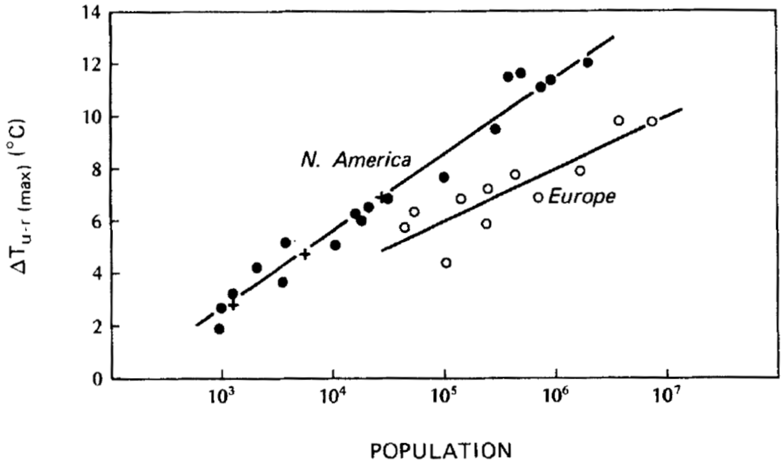

Figure 2.5: Relationship between population and peak UHI intensity (Oke, 1982)

So parametrisation of Q_F is dependent on the city (both its structure and its geographical location) and should be differing by seasons as well. For an easier implementation however, in this thesis Q_F is held constant throughout the year but it is dependent on the land use class. The values are taken from Stewart et al. (2014) who state that their numbers are valid for cities all over the world as they are based on measurements and estimations from sites worldwide. Section 4.3.2 goes into more detail as to what the actual values of Q_F are.

2.3 Climate Change and Land Use Change in Cities

As this thesis analyses the combined effects of urban planning and climate change, some modelling studies concerning one or both of these effects are presented in this section.

Parts of the studies investigate the effects of a change of external parameters on climate of specific cities by analysing single days. Sailor (1995), e.g., examined the influence of increased albedo or vegetative cover this way. Schoetter et al. (2013) on the other hand estimated the effects of both climatic changes (increased air temperature, water vapour pressure, radiant temperature and wind speed) and increased street canyon width and building height.

Regional climate simulations on longer time periods concerning both climate change and urban climate have already been conducted by Hamdi et al. (2013) for Brussels, additionally by Kusaka et al. (2012) for several Japanese cities and by Adachi et al. (2012) for Tokyo alone. Here, the impacts of both climate change and urbanisation were analysed, just like this thesis is going to do.

The German Weather Service (*Deutscher WetterDienst*, DWD) has carried out modelling studies concerning the combined effects of climate change and urbanisation for Frankfurt (Früh et al., 2011), Cologne (Grothues et al., 2012) and Jena (Hoffmann et al., 2014). However, the urban climate model was not used in a coupled climate simulation, but rather for statistical downscaling of climate variables (air temperature, humidity and wind speed) to variables relevant for urban climate.

Besides dynamical downscaling, which is one method of regional climate simulations, some studies use statistical downscaling of global climate simulations. Wilby (2008) conducted a statistical downscaling of several general circulation models (GCMs) to calculate ozone concentrations and nighttime UHI intensity for the 2050s in London. Hoffmann et al. (2012) developed a statistical model to calculate future UHI intensity in Hamburg from variables of regional climate projections. They assumed the statistical relationship between predictor and predictand to be equal for both present and future. However, McCarthy et al. (2010) already disproved this assumption. They analysed the interrelation of doubled CO_2 and urban climate based on global simulations incorporating a single-layer urban model concluding that UHI intensity changes with increased CO_2. This implies that explicit simulations incorporating both climate change and the effects of cities on local climate are needed to obtain projections of future urban climate.

3. Description of the Stuttgart Metropolitan Area (SMA)

This chapter provides an overview on the climatic situation of the Stuttgart Metropolitan Area (SMA). Additionally, it describes how the different land use distributions for the scenarios were obtained. The term SMA as used here comprises the city of Stuttgart plus some surrounding area with the dimensions of about 22×23 km.

3.1 Geography of the SMA

The information contained in this section is taken from Landeshauptstadt Stuttgart (2008). The German state of Baden-Württemberg that the SMA lies in, belongs to the transitional zone of submaritime and subcontinental climate, but the dominant component determining the state's climate is its orography. The Black Forest and the Swabian Jura (parts of the low mountain range (*Mittelgebirge*), see Fig. 3.1) cause windward and leeward effects that strongly influence all climatic elements. Additionally, hillsides facing south and southwest receive an increased amount of solar irradiance.

Most of the SMA lies in the Neckar basin with the Black Forest to the southwest, the Swabian Jura to its southeast, the Schurwald and Swabian Forest to the east, Stromberg and Heuchelberg area to the northwest and the Swabian-Franconian Forest to its northeast. The city centre of the SMA is located in a basin (so called *Kessellage*) delimited by the Filder plateau to its southwest with maximum elevation differences of about 260 m. The Nesenbach valley cuts through it from southwest to northeast and the Neckar enters the SMA from southeast leaving it in the northeast. The *Kessellage* creates a special climate with reduced wind speed and increased temperatures compared to a plain. Combined with the general urban influences on local climate (chapter 2), temperature differences of up to 7 °C compared to the surroundings can occur. Besides the reduction of wind speed and the increase in temperature, the *Kessellage* favours the formation of low-level temperature inversions through cold air flow from the hillsides to the bottom of the basin. All of these effects lead to bad air quality as the exchange of polluted urban air with clean suburban or upper-level air is reduced.

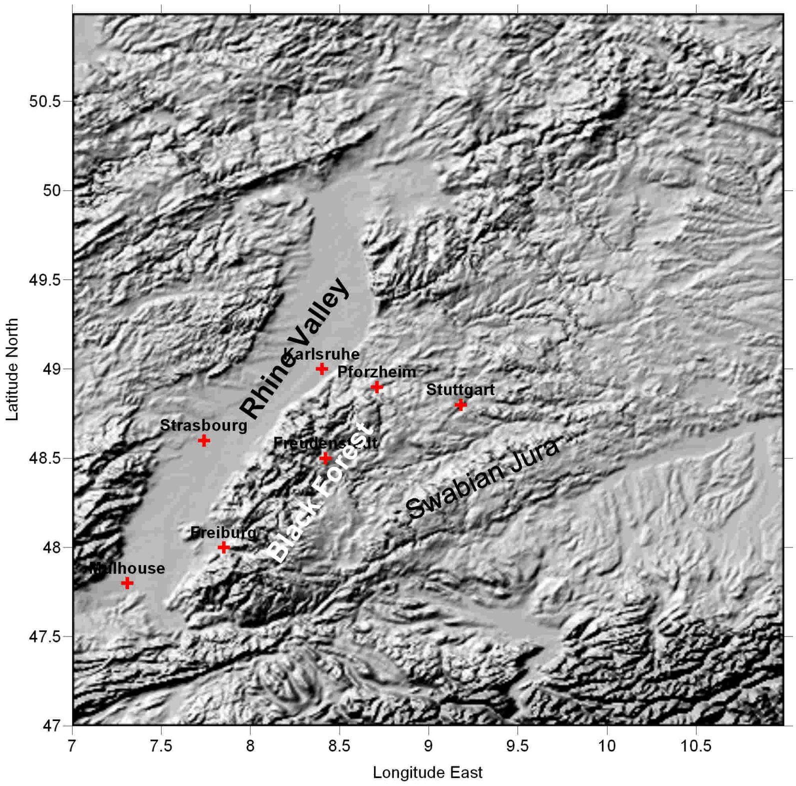

Figure 3.1: Orography of Baden-Württemberg and its surrounding area with SMA (Stuttgart) in the centre, courtesy of Gerd Schädler

3.2 Climate of the SMA

3.2.1 Temperature

In Stuttgart-Schnarrenberg, which is a DWD-station in the north of the city (see Fig. 3.2 b), January is the coldest month with on average 1.3 °C for the climatological period 1971-2000 (Fig. 3.2 a). The warmest month is July with an average temperature of 19 °C and the annual mean temperature is 9.9 °C.

The spatial distribution of the mean number of summer days (daily maximum 2 m temperature $T_{max} \geq 25$ °C) per year is clearly related to topography (Fig. 3.2 b): in the lower areas of the Neckar valley, more than 45 summer days occur, in the higher elevated Filder plateau to the southwest of the domain, less than 35 days exceed 25 °C on average.

According to KLIWA (2013), mean temperature in the Neckar region has increased significantly by 1.0 °C during hydrological summer (May-October) and by 1.3 °C during winter (November-April) from 1931 to 2010. The difference is larger in winter than in summer, but the rise in temperature has become steeper for summer than for winter during the last years.

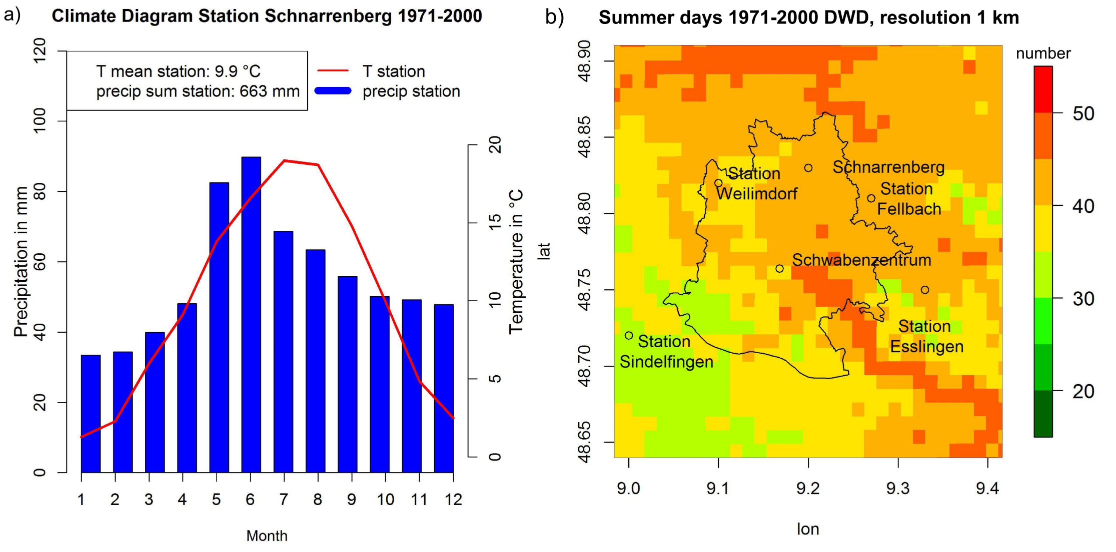

Figure 3.2: Climate diagram of station Stuttgart-Schnarrenberg (a) and distribution of summer days ($T_{max} \geq 25\,°$ C) in the SMA (b), both for period 1971-2000, courtesy of Julia Hackenbruch

3.2.2 Precipitation

The leeward location of the SMA causes a comparatively low precipitation amount. A large amount of relief rainfall occurs at the windward side of Swabian Jura and Black Forest (Landeshauptstadt Stuttgart, 2008) resulting in a low average annual precipitation amount of 663 mm at Stuttgart-Schnarrenberg in the leeward area of the two low mountain ranges. Maximum precipitation amount occurs in June (Fig. 3.2 a) as here often locally induced convective precipitation develops which is not that affected by the SMA's leeward location. In winter, when precipitation is mostly caused by synoptic conditions, precipitation amounts in the SMA are lowest.

For the period of 1931-2010, KLIWA (2013) reports an increase in wintertime precipitation by 16.6 % and a small decrease in summertime precipitation. However, both numbers are not very significant with the wintertime trend having a higher significance level than the summertime trend.

3.2.3 Wind

Germany lies within the westerlies, the prevailing wind direction is west to southwest. Due to its undulating terrain, wind directions in the SMA may differ tremendously from the main direction (Landeshauptstadt Stuttgart, 2008). Fig. 3.3, which is based on measurements at the station Schwabenzentrum (for location, see Fig. 3.2 b) for the period 1987-2000, shows this for the wind distribution during daytime. The most common wind direction is southwest, where also the strongest winds occur. However, a secondary maximum exists for winds from northeastern directions. The station is situated in the centre of the city where the Nesenbach valley is oriented from southwest to northeast.

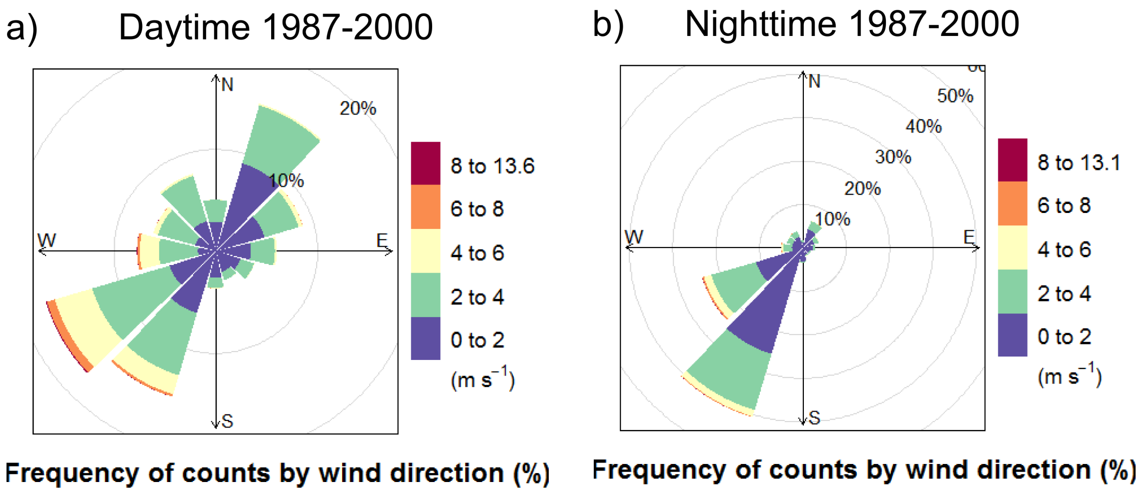

Figure 3.3: Mean wind roses for station Stuttgart Schwabenzentrum (for location, see Fig. 3.2 b) 1987-2000 during the day (8:00-19:00, a) and during the night (20:00-7:00, b), courtesy of Julia Hackenbruch

So the secondary maximum probably is caused by a channelling of upslope winds and possibly an urban breeze along the Nesenbach valley. During the night, on the other hand, there are hardly situations with wind directions other than southwest (Fig. 3.3 b). This is when the channelled cold air flow or mountain wind from the Filder plateau adds up to the channelling of the large-scale flow (Landeshauptstadt Stuttgart, 2010).
Wind speeds of sometimes less than 1.7 m/s make the SMA one of the least windy cities of Germany (Nationalatlas, 2003 in Landeshauptstadt Stuttgart, 2008)

3.2.4 Solar Radiation

As the SMA is located in the south of Germany, values for global radiation are higher than in most of the rest of the country. Additionally, the leeward location of the SMA causes a high mean annual sum of global radiation of 1075 - 1125 kWh/m^2 (Landeshauptstadt Stuttgart, 2008). This is caused by enhanced cloud and precipitation formation at the windward sides of Black Forest and Swabian Jura resulting in less cloudiness at their leeward side where the SMA is located (Landeshauptstadt Stuttgart, 2008).
Sunshine duration is dependent on the cloudiness as well. Thus, a high mean annual sunshine duration of about 1600 - 1700 hours is observed in the SMA (Landeshauptstadt Stuttgart, 2008).

3.3 Distributions of Land Use Classes for the SMA

3.3.1 Reference Land Use

The *Umweltamt* (environmental office) of Stuttgart provided land use data of the city as vector files. The land use classes consisted of mixed, deciduous and coniferous forest, open space, business, tarmac, densely built-up and open-set built-up areas. To be used in Veg3D, the land use data had to be rasterised and afterwards were aggregated on a grid of approximately 1 km grid spacing.

The grid spacing of 1 km was used since initially it was intended to run the coupled simulations on this resolution. But due to computational problems there was not enough time to run coupled simulations of this high resolution. Still, some stand-alone simulations have been conducted with a horizontal grid spacing of 1 km (chapter 5).

For land use outside of the city boundaries, GLC2000 data interpolated onto the grid of the city's land use were added. GLC2000 land use data were obtained from the instrument VEGETATION onboard the satellite SPOT 4 and have a resolution of 1/112° which corresponds to 1 km at the equator (Bartholomé and Belward, 2005). GLC2000 data often provided several land use classes for one grid point. In case that one of the two land use classes was urban, this grid point was assigned LCZ 6 (for a detailed description of the urban land use classes implemented in Veg3D, see Fig. 3.4 and section 4.3.2).

For use with Veg3D, preliminary land use classes of *Umweltamt* and GLC2000 had to be converted to Veg3D land use classes (Fig. 3.5). Therefore, GoogleMaps satellite images of the SMA were used when a distinction more precise was needed. For example, *Umweltamt* class open space was assigned to one of the Veg3D classes special crops, agriculture, meadows, grassland and LCZ 8 (this was one grid point at the airport). Urban area of GLC2000 was assigned LCZ 5 if the grid point was 100 % urban; in case that the grid point consisted of 50 % urban area, it was assigned LCZ 6. No grid point was assigned LCZ 2 assuming that blocks of houses do not cover significant areas outside

Intensification

LCZ class	description by Stewart and Oke (2012)	interpretation for SMA
LCZ 6	open low-rise	single-family houses, one to two storeys
LCZ 5	open mid-rise	multi-storey houses, two to three storeys
LCZ 2	compact mid-rise	blocks of houses, about four storeys
LCZ 8	large low-rise	office buildings
LCZ 10	heavy industry	industry

Figure 3.4: Explanation of LCZs used in this thesis: the original description by Stewart and Oke (2012) and the interpretation for this analysis. The arrow indicates the growing degree of urbanisation or industrialisation, respectively.

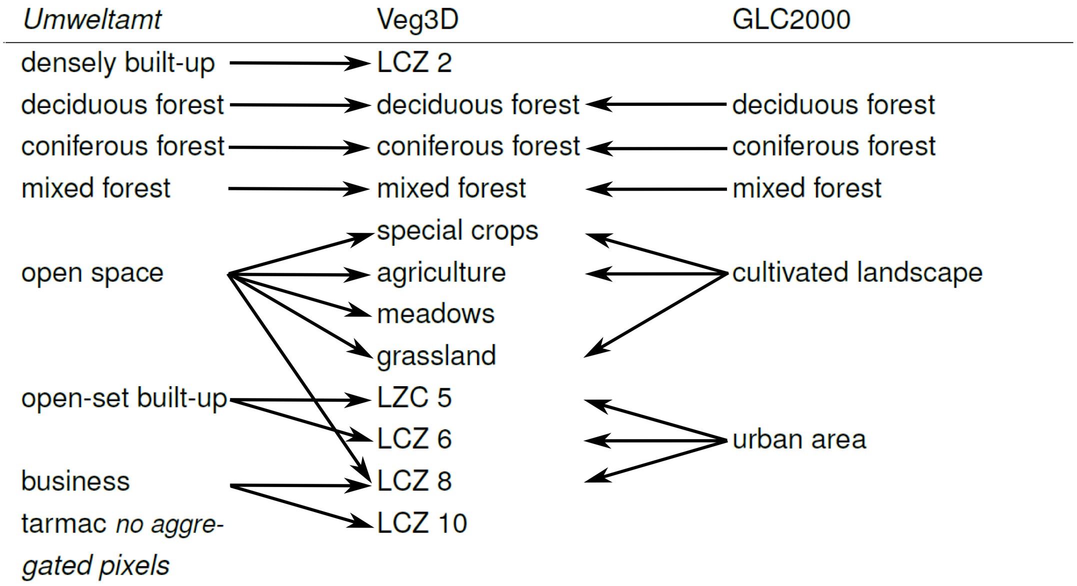

Figure 3.5: Assignment of Umweltamt *and GLC2000 land use classes to Veg3D land use classes through examination of GoogleMaps satellite images*

the city. A comparison of both datasets for the city of Stuttgart (inside the black polygon in Fig. 3.6) reveals quite some discrepancies. Considerably larger areas of the GLC2000 dataset are covered by urban land use (Fig. 3.6 a), but the *Umweltamt* dataset is differentiated between more land use classes (Fig. 3.6 b). A closer look onto the figure suggests that GLC2000 contains too many built-up grid points, *Umweltamt* on the other

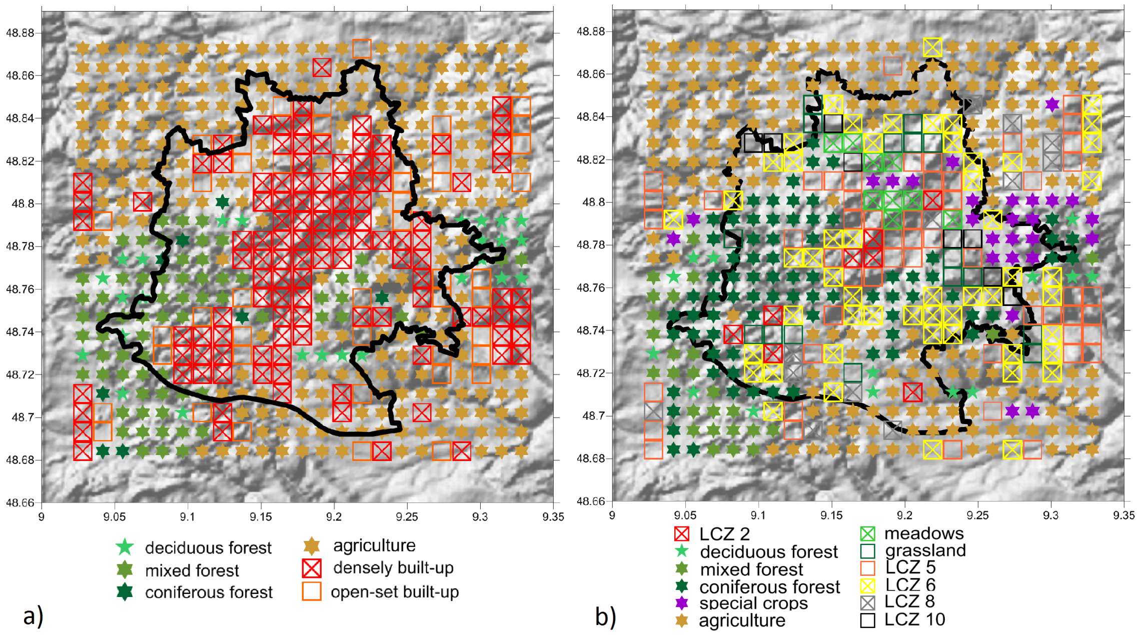

Figure 3.6: Land use of (a) GLC2000 and (b) Umweltamt *on orography of SMA. Only consider city centre inside the black polygon as the surrounding land use is GLC2000 for (b), too.*

hand possibly a bit too few. Still, *Umweltamt* data are used for this thesis as those are supposed to be the more accurate data.

The soil type distribution is taken from the Harmonized World Soil Database (HWSD, Nachtergaele et al., 2008) which merges various soil databases and has the same resolution as GLC2000 data. Amongst other variables, HWSD provides top (0 to 30 cm depth) and sub (30 to 100 cm depth) soil classes. These classes were again aggregated on the land use grid.
HWSD also indicates grid points where there is urban area. These grid points do not have a top and sub soil then. For consistency, I assigned grid points that were urban areas according to HWSD, but not according to the land use distribution to the soil class loam. Also, both top and sub soil below a grid box with an urban land use class according to the land use distribution are assigned loam.

3.3.2 Future Land Use, Red Scenario

For the future red scenario land use, an intensified urbanisation is assumed. The changes of land use distribution were performed according to the following criteria:

- all grid boxes of class LCZ 5 (multi-storey houses) change to class LCZ 2 (blocks of houses)
- all grid boxes of rural land use classes with at least two neighbours of classes LCZ 8 or 10 (business or industry) change to this neighbouring class
- the rest of the grid boxes of rural classes with at least two neighbours of urban classes (LCZ 2, 5, 6, 8 or 10) change to class LCZ 6 (single-family houses)
- all grid boxes of class LCZ 6 with at least four urban neighbours change to LCZ 5

Fig. 3.7 shows the land use distribution for the reference runs (a) and the red scenario (b). As intended, the area of urban land use classes has grown considerably. In contrast to the green scenario, for the red scenario only a modification in land use distribution is assumed. There is no additional adjustment in the parametrisation of the land use classes.
The distribution of soil types is not considered to change in the future, apart from keeping the consistency of grid points belonging to urban areas according to either HWSD or the land use distribution (see end of section 3.3.1).

3.3.3 Future Land Use, Green Scenario

For the green scenario, a combination of changing land use distribution and changing properties of the urban land use classes was applied. The change of land use distribution only consists of reforestation of an area in the southeast of the domain. Here, 49 grid

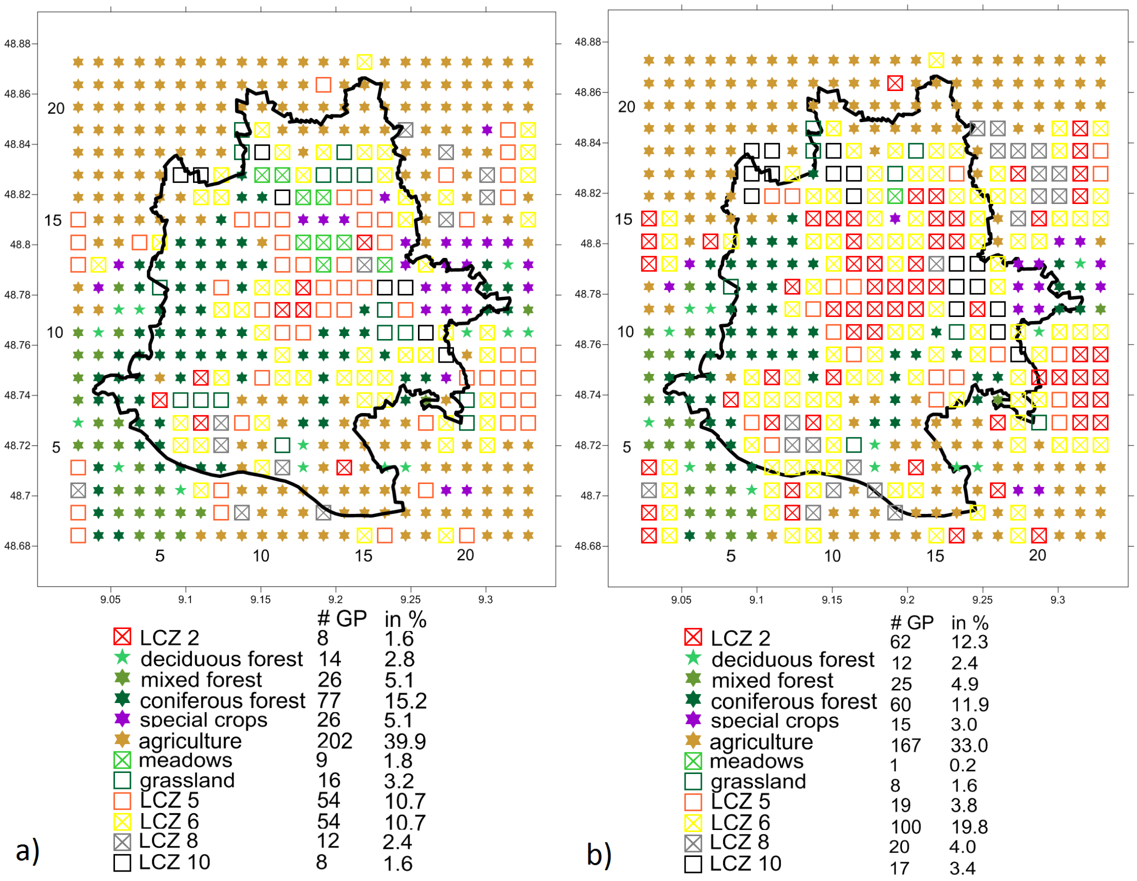

Figure 3.7: Land use in Stuttgart for control run and reference projection (a) and red scenario (b)

boxes of the class agriculture were converted to mixed forest on the 1 km-grid.

The considerations for changing variables of the urban land use classes were an increase in green space, planting of additional trees and reduced energy consumption. These assumptions lead to an increase in the pervious surface fraction σ_f and a decrease in anthropogenic heat input Q_F of the urban land use classes.

Modifications of different parameters were tested in stand-alone mode. This is described in section 5.3.1.

3.3.4 Land Use on 2.8 km-Grid

The final coupled simulations were run on a 2.8 km-grid which required the aggregation of the land use distribution from the 1 km-grid to the 2.8 km-grid. Thus, the land use distributions of Fig. 3.8 evolved.

Fig. 3.9 displays the frequency distribution of the land use classes for the different scenarios. It shows that for the red scenario fewer grid points are assigned rural land use classes, but a larger number of grid points is assigned more intensified urban land use (the change from LCZ 5 to LCZ 2) or urban land use at all (LCZ 6). Additionally, only for the red scenario one grid point is assigned LCZ 10 with the high amount of

$Q_F = 300$ W/m^2. Compared to the reference land use, for the green scenario only the distribution of mixed forest and agriculture changes as described in section 3.3.3.

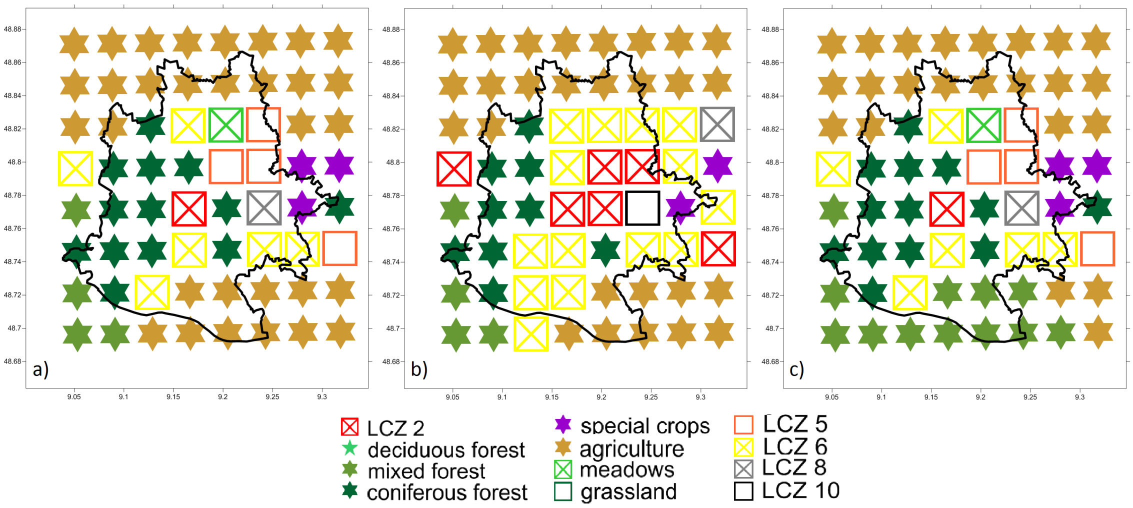

Figure 3.8: Land use on 2.8 km-grid for the different scenarios: reference land use (a), red scenario (b) and green scenario (c)

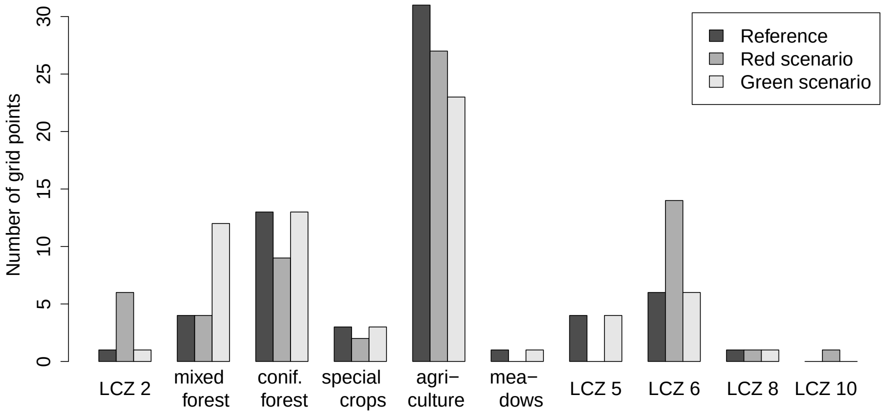

Figure 3.9: Frequency distribution of land use classes on 2.8 km-grid for the different scenarios

4. Description of Models

This chapter introduces the different models that have been used for this thesis as well as the modifications of the SVAT-model. Also, some urban parametrisation schemes are presented.

4.1 Regional Climate Modelling

General Circulation Models (GCMs) are able to represent global changes in large-scale features like the global temperature for the entire Earth. But due to high computational costs, their horizontal grid spacing is limited to the range of about 100-200 km at present (Rummukainen, 2010). Regional Climate Models (RCMs) provide a physically consistent method to dynamically downscale results of GCMs to smaller scales. Their horizontal grid spacing mostly lies in the range of 20 km, but can be as low as a few km (e.g., Fosser, 2013; Knote et al., 2010).

Thus, orographic effects and small scale processes like convection can be described more accurately. These high-resolution results allow the assessment of regional and local climate features like local wind systems, orographic shadowing and precipitation.

Fig. 4.1 displays the topography of Germany for three different resolutions: 200 km, which is the grid spacing of GCMs, 50 km, the grid spacing of a coarse RCM and 2.8 km, the grid spacing that is used in this thesis. It becomes clear that for an assessment of precipitation, where orographic effects can play a major role, the high resolution of the topography of an RCM can be expected to provide better results.

In contrast to GCMs which model the entire atmosphere of the Earth, RCMs are limited area models. Thus, they need boundary conditions which are usually provided by GCM-results. This is called nesting an RCM into a GCM. Initial conditions are also given by the global simulation. The lateral boundaries are updated every 3 or 6 hours. The soil, however, is usually only initialised in the beginning of the simulation and not updated like the boundaries of the domain.

COSMO

For this thesis, the COSMO-model (COnsortium for Small-scale MOdelling) is used as regional climate model. It has been developed at the DWD and can be run both in Numerical Weather Prediction (NWP) and climate mode (COSMO-CLM: COSMO model

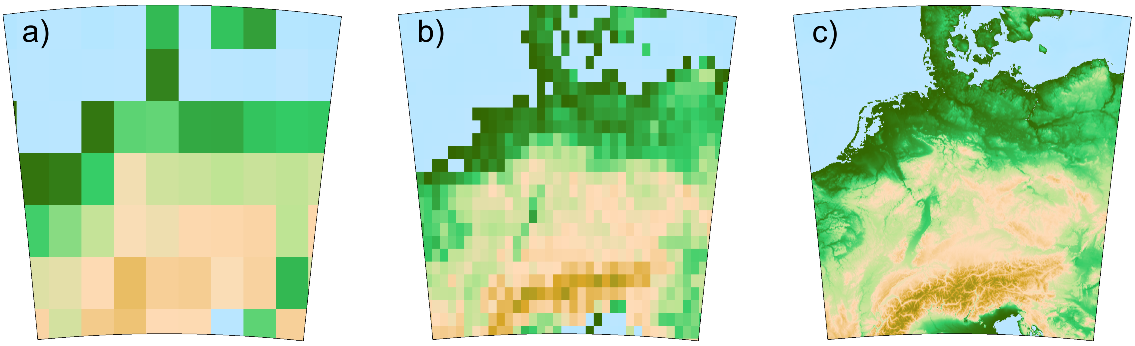

Figure 4.1: Topography of Germany at different resolutions: (a) 200 km, (b) 50 km, (c) 2.8 km, courtesy of Hans Schipper

in CLimate Mode). One difference between the two modes is the handling of constant external parameters like the Leaf Area Index (LAI)[1] or the amount of plant cover. In NWP-mode, the model is run for short periods of time, thus these parameters are held constant. In COSMO-CLM, the parameters differ throughout the year and either have to be provided to the model or be calculated in the SVAT-model (Kohlhepp, 2009). Furthermore, only NWP-mode uses data assimilation. But the basis of the model consisting of dynamics, numerics and parametrisations is the same for NWP and climate mode.

COSMO is a non-hydrostatic model which allows a more accurate calculation of the vertical acceleration (Adrian and Frühwald, 2002). Thus, theoretically there is no limit to very high resolution. The expense of not using the hydrostatic assumption is a smaller time step, as for example sound waves are filtered by the hydrostatic assumption and now need to be resolved partly (Doms, 2011). The higher resolution allows the explicit calculation of deep moist convection superseding parts of the convection parametrisation and, as stated before, a better resolution of topography enables a better representation of orographically induced convection (Doms, 2011).

COSMO is formulated on a rotated grid with the equator and the prime meridian in about the centre of the modelling domain. In the vertical, a generalised terrain following height coordinate is used. The model is based on the primitive thermo-hydrodynamical equations describing compressible flow in a moist atmosphere. Processes that are not resolved by these equations are described by various parametrisation schemes (Doms, 2011).

---

[1] LAI is defined as the area of green leafs per unit ground area and influences the amount of evapotranspiration caused by the vegetation

4.2 Modelling Urban Climate

One possibility of analysing climate in a city is the use of specific urban parametrisations. Some of these are presented in this section.

An example of a rather sophisticated scheme is the Building Effect Parametrisation (BEP) by Martilli et al. (2002). It parametrises the effects of buildings on momentum, temperature and the turbulent kinetic energy in a mesoscale atmospheric model without explicitly resolving individual buildings. Also, radiation trapping and shadowing effects of street canyons are taken into account and the buildings' heights cause changes in the turbulent length scales. But as so many processes need to be computed for this model, it requires a high amount of computing time. When applying the BEP, the modified routine is about two times slower than the original one.

The DWD has developed the urban climate model MUKLIMO_3 (*Mikroskaliges Urbanes KLImaMOdell*, microscale urban climate model) to analyse heat stress situations in cities (Früh et al., 2011). Urban land use is divided into 10-13 classes (for Frankfurt there are more classes due to its unique financial district). The impacts of urban land use on air flow and radiation are described by parametrisations, vegetation is regarded in a three-layer model and heat and humidity exchange of the soil are calculated. But the model does not represent precipitation formation, so it can only be used for non-precipitation events or days. Some applications of this model have been presented in section 2.3.

The general canopy approach by Best (1998) (as cited in Best, 2006) is the least complex kind of urban parametrisation. It consists of a simple energy balance similar to that of vegetation. Street canyons or roofs are not treated specifically, so the entire urban area is handled as one canopy. This simple approach can easily be implemented into a mesoscale model and needs only small amounts of computing time. It has been in operational use in the Met Office Mesoscale model since November 2000.

The SVAT-model Veg3D, which is used for urban parametrisation in this thesis, similarly treats land use as a single layer between the soil and the atmosphere exchanging energy and mass with both neighbouring layers. Additionally and in contrast to Best's approach, anthropogenic heat input is taken into account and there is a more precise differentiation between different types of urban land use. The following section 4.3 goes into detail on these issues.

I use a less sophisticated way of parametrising urban effects on climate as the goal is to obtain simulation results for climatological time periods which would be computationally too expensive when using an urban model of higher resolution.

4.3 Veg3D

4.3.1 Description of the Model

The SVAT-model coupled to COSMO-CLM in this thesis is Veg3D. The coupling has been implemented by Marcus Breil. Veg3D has been developed by Schädler (1990) and incorporates an explicit vegetation layer. This layer treats vegetation according to the 'big leaf' concept, meaning that vegetation is considered as one homogeneous and massless layer between soil and atmosphere. Turbulent flows, canopy air temperature and humidity within the layer are calculated by balancing energy and mass fluxes. Additionally, short and long wave radiation balances are altered by the vegetation layer.

Different types of vegetation are represented by the land use classes implemented in Veg3D. They determine various parameters as, e.g., LAI, albedo, displacement height and root depth (see also Tab. 4.1). Many of these variables change throughout the year between specified minimum and maximum values. For more information on Veg3D, see, e.g., Meißner (2008) and Braun (2002).

4.3.2 Modifications of the Model

For a better representation of urban areas in Veg3D, some modifications of the model have been performed. New urban land use classes have been added and anthropogenic heat input has been included in the model.

Land use classes

The default land use classes in Veg3D were bare soil, urban area, water, deciduous forest, mixed forest, coniferous forest, special crops, agriculture, meadows and grassland. For an investigation of the impact of built-up areas on urban climate, a more precise description of urban areas is needed. Stewart and Oke (2012) developed a system of land use classes to characterise both rural and urban sites on all continents (Fig. 4.2). Some of these Local Climate Zones (LCZs) are used in this thesis to define two additional urban areas (LCZ 5: not block of houses but mid-rise multi-storey houses, LCZ 6: single-family houses), one class for large but flat buildings like office buildings (LCZ 8) and one class representing industry including factories (LCZ 10, see also Tab. 4.1 and Fig. 4.3). Also, some parameters of the Veg3D class urban area (now block of houses) were adopted from LCZ 2 and all values for anthropogenic heat input were taken from Stewart et al. (2014). Parameters adopted from LCZs for all urban classes are: albedo, emissivity, roughness length[2], displacement height[3], pervious surface fraction and anthropogenic heat input. Additional parameters needed for Veg3D (e.g, LAI, minimum stomatal resis-

---

[2] Roughness length accounts for the roughness of the ground or vegetation

[3] Displacement height considers the effects of extended obstacles on the atmospheric flow. The addition of roughness length and displacement height results in the height where the mean wind is zero.

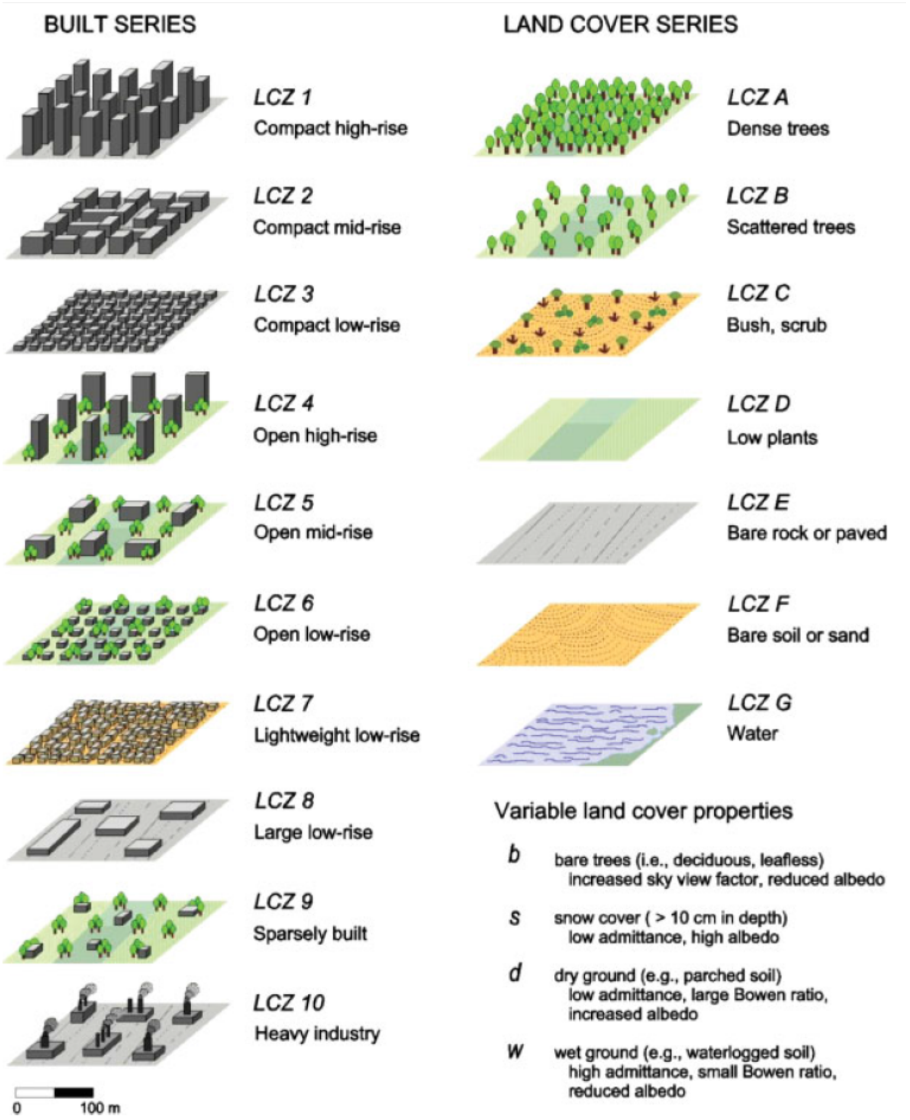

Figure 4.2: The Local Climate Zones (LCZ) developed by Stewart and Oke (2012)

tance[4]) were estimated from the original class urban area. The mentioned parameters are listed in Tab. 4.1 for all land use classes relevant in the SMA.

Anthropogenic Heat Input

Anthropogenic heat input (Q_F) has been implemented in Veg3D by adding Q_F to an undisturbed energy balance according to Eq. 2.1. In Veg3D, energy advection ΔQ_A is not considered and energy storage ΔQ_S is treated as ground heat flux which leads to the following equation:

$$Q^* + Q_F = Q_H + Q_E + \Delta Q_S \tag{4.1}$$

---

[4] Minimum stomatal resistance controls the amount of transpiration by the vegetation

Q_F is added to the energy balance of the surface since input of anthropogenic heat mostly occurs close to the ground.

The values of Q_F for the different urban land use classes were taken from Stewart et al. (2014) and are listed in Tab. 4.1. They compare well with those quoted in section 2.2. Only the 300 W/m^2 for LCZ 10 seem a bit too high for industry in the SMA. However, I still used it to test what the model result of such an extreme additional heat input would be. It can be expected that 300 W/m^2 as anthropogenic heat input not only elevate temperature near the ground, but also might trigger local convection.

For the future green scenario, Q_F was reduced to 60 % of the initial values and the high value of LCZ 10 was reduced further, but LCZ 10 only occurs in the red scenario projection of the coupled simulations anyway.


http://commons.wikimedia.org/wiki/File:Stuttgart_vom_Fernsehturm_1.jpg

http://commons.wikimedia.org/wiki/File:Stuttgart-Gaisburg_Panorama.jpg

Figure 4.3: Photos of the SMA, above: city centre with dense development (LCZ 2) in the foreground and multi-storey houses (LCZ 5) in the background, below: Stuttgart-Untertürkheim with production plant (LCZ 10) in the Neckar valley

Parameter	Symbol	Unit	LCZ 2	LCZ 5	LCZ 6	LCZ 8	LCZ 10	deciduous forest	mixed forest	coniferous forest	special crops	agriculture	meadows	grassland
Albedo	α_f	1	0.1675	0.1575	0.1625	0.1725	0.1475	0.15	0.11	0.13	0.18	0.2	0.2	0.18
Emissivity	ϵ_f	1	0.92	0.92	0.92	0.92	0.92	0.96	0.97	0.96	0.97	0.96	0.96	0.96
Roughness length	z_0	m	0.905	0.62	0.31	0.34	0.37	0.7 - 0.8	1.0	0.85 - 0.9	0.25 - 0.3	0.02 - 0.07	0.02 - 0.03	0.07 - 0.08
Displacement height	d	m	10.0	6.9	3.0	4.0	5.5	8.0 - 9.0	12.0	10.0 - 10.5	1.5 - 2.0	0.1 - 0.4	0.1 - 0.15	0.35 - 0.4
Pervious surface fraction	σ_f	1	0.1	0.3	0.4	0.15	0.1	0.7 - 0.95	0.9	0.8 - 0.95	0.7 - 0.8	0.15 - 0.8	0.9 - 0.95	0.75 - 0.85
Anthropogenic heat input - red scenario	Q_F	W/m^2	35.0	15.0	10.0	40.0	300.0	0.0	0.0	0.0	0.0	0.0	0.0	0.0
Anthropogenic heat input - green scenario	Q_F	W/m^2	21.0	9.0	6.0	24.0	50.0	0.0	0.0	0.0	0.0	0.0	0.0	0.0
Leaf area index	LAI	1	1.0 - 2.0	1.0 - 2.0	0.75 - 3.5	0.5 - 1.0	0.5 - 1.0	0.5 - 8.0	9.0 - 13.0	4.0 - 10.0	0.5 - 5.0	1.0 - 3.5	2.0 - 4.0	1.5 - 4.0
Minimum stomatal resistance	r_{min}	s/m	250.0	200.0	200.0	250.0	250.0	120.0	120.0	120.0	180.0	100.0	150.0	150.0

Table 4.1: Parameters for all relevant land use classes of Veg3D. Albedo, emissivity, roughness length, displacement height, pervious surface fraction and anthropogenic heat input - red scenario for the LCZs are given in Stewart et al. (2014), LAI and minimum stomatal resistance were estimated from Veg3D's original class urban area. For those parameters that follow an annual cycle, the range between their minimum and maximum is given.

5. Stand-Alone Simulations of Veg3D

For first tests of the implementation of the modifications of Veg3D, several stand-alone runs were conducted. This means that the SVAT-model is driven by atmospheric data (provided by, e.g., a former coupled simulation), but is not able to influence the model atmosphere.

5.1 Test of Implementation of Anthropogenic Heat Input

To test the implementation of the anthropogenic heat input Q_F in Veg3D, a stand-alone simulation for the year 1984 with a horizontal grid spacing of 1 km was conducted for the SMA as shown in Fig. 3.7 a.

Fig. 5.1 displays the weekly mean of the soil temperature for land use classes LCZ 2 with $Q_F = 35$ W/m^2 (a and b) and LCZ 10 with $Q_F = 300$ W/m^2 (c and d) as well as the mean over all grid points of the simulation domain (e and f). To the left, the average over the first four layers (between the surface and a depth of 28 cm) is shown, to the right, the second lowest, ninth layer at a depth of 5.74 m is presented. Magenta marks the soil temperature of the run with Q_F, blue indicates the soil temperature of the simulation without Q_F. The difference between the runs with Q_F and without Q_F is shown in Fig. 5.2 with the same structure as in Fig. 5.1.

For LCZ 10, the temperature difference is largest due to its high amount of Q_F. In the upper soil layers, this causes a temperature increase by up to 35 K (Fig. 5.2 c). In the ninth soil layer, the rise of temperature amounts to about 7 K after one year. The very high amount of Q_F might be too large for the SMA, but I still used it to test the maximum influence of Q_F on the atmosphere.

Temperatures for the entire domain are similar to those of LCZ 2. It is about 3 K higher for the run with Q_F in the upper soil layers and after one year, the difference is nearly 1 K in the ninth layer.

Overall, this stand-alone simulation shows that the implementation of Q_F and the additional land use classes was successful. Including Q_F into the energy balance of the surface elevates soil temperatures. An increase in soil temperature was expected as adding Q_F according to equation 4.1 results in elevated ground heat flux ΔQ_S whereby soil temperatures rise. It is assumed that in a coupled simulation, air temperature will increase as well, since the atmosphere also interacts with the additional heat flux.

One notable aspect in Fig. 5.2 b, d and f is that the increase in soil temperature at a depth of 5.74 m has not converged on a constant value after one year. In the upper layers, convergence occurs after about 15 weeks (Fig. 5.2 left). This illustrates that it takes a considerable amount of time until changed forcings (in this case the addition of Q_F) reach the lower soil layers completely. For this reason, a spin-up of the soil alone is desirable to reach an equilibrium state of the soil temperature and water content. The following section 5.2 covers this issue.

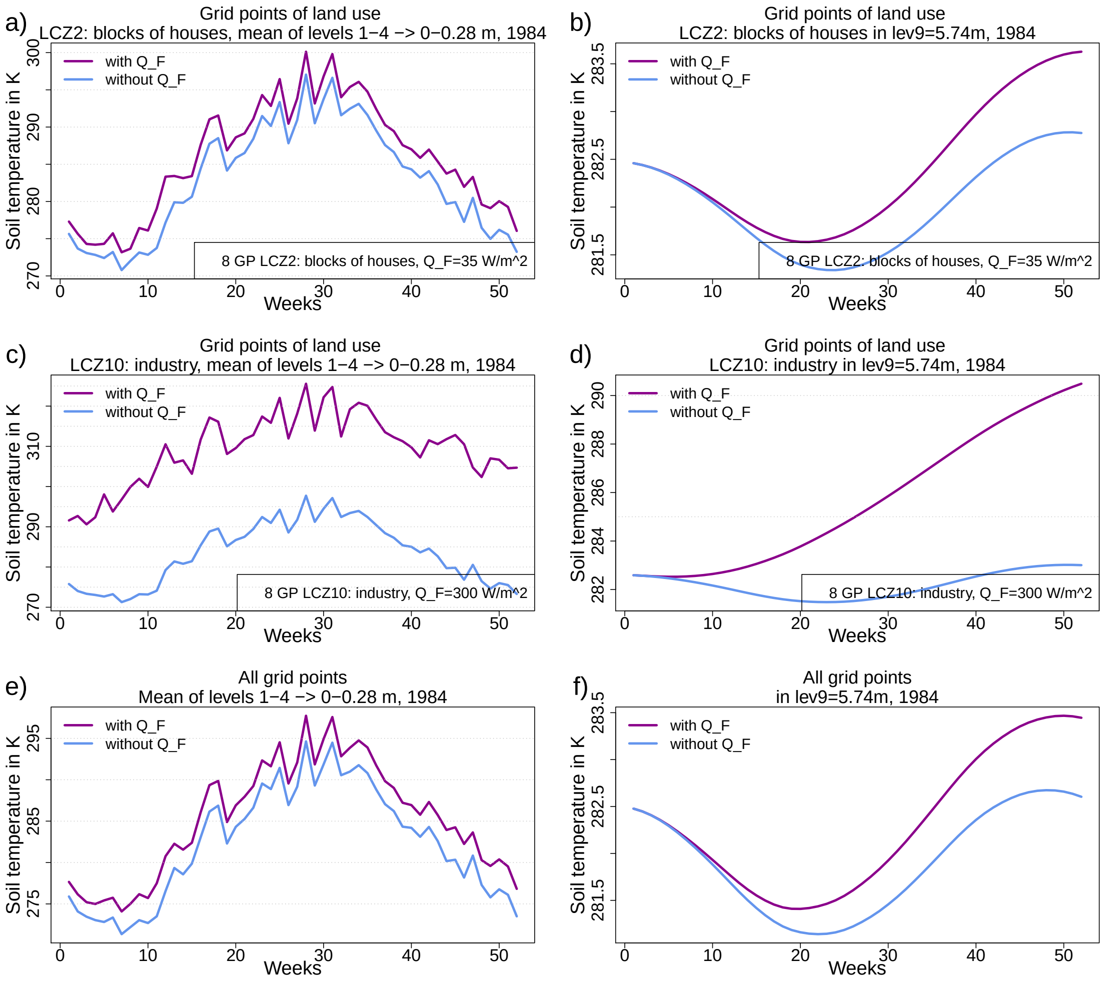

Figure 5.1: Weekly and areal mean of soil temperature for run with and without Q_F for year 1984 for grid points of land use class LCZ 2 (a) and (b), LCZ 10 (c) and (d) and averaged over the entire domain (e) and (f). Mean over the upper four soil layers (a, c, e) and in the second lowest layer (b, d, f).

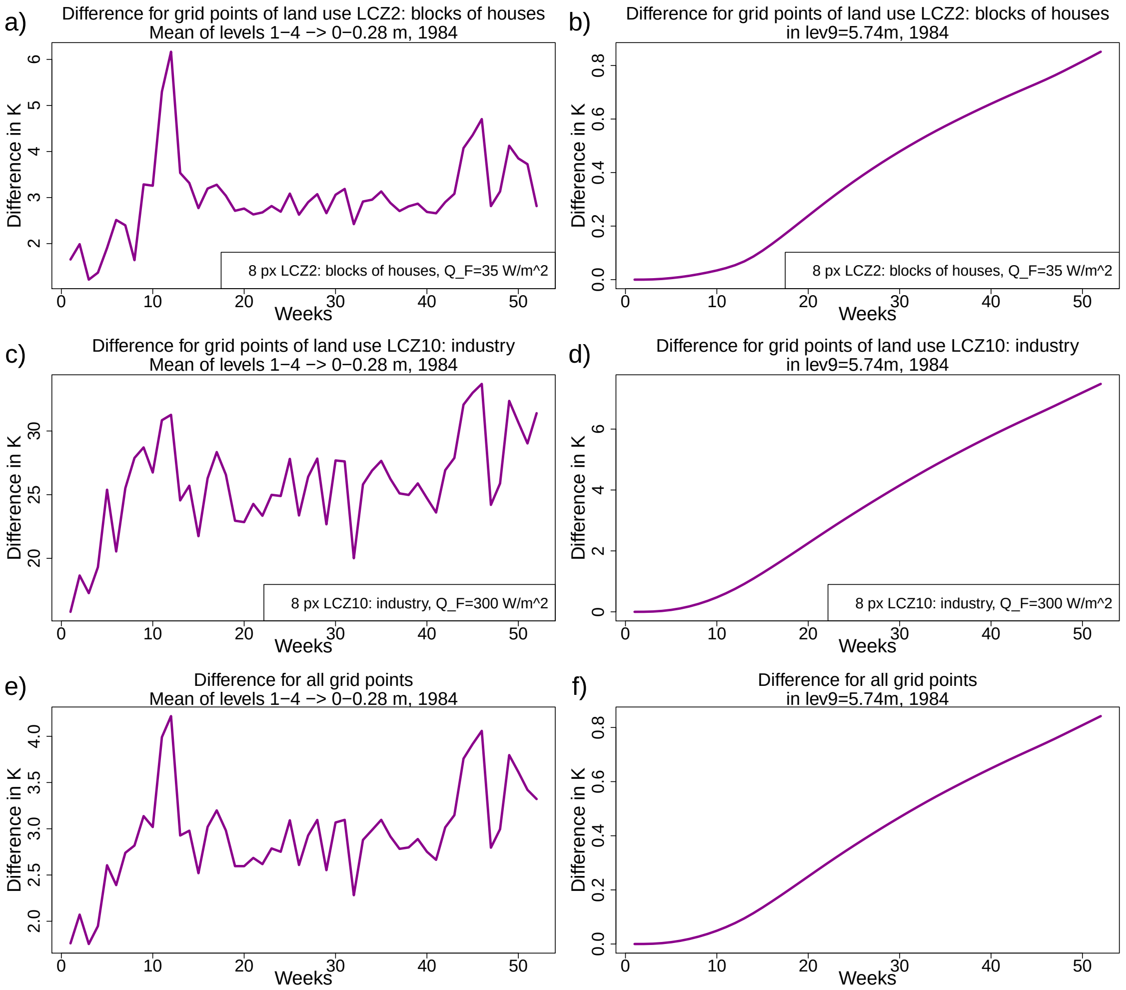

Figure 5.2: Same as Fig. 5.1, but for the difference of the weekly and areal mean of soil temperature for the run with and without Q_F for the year 1984

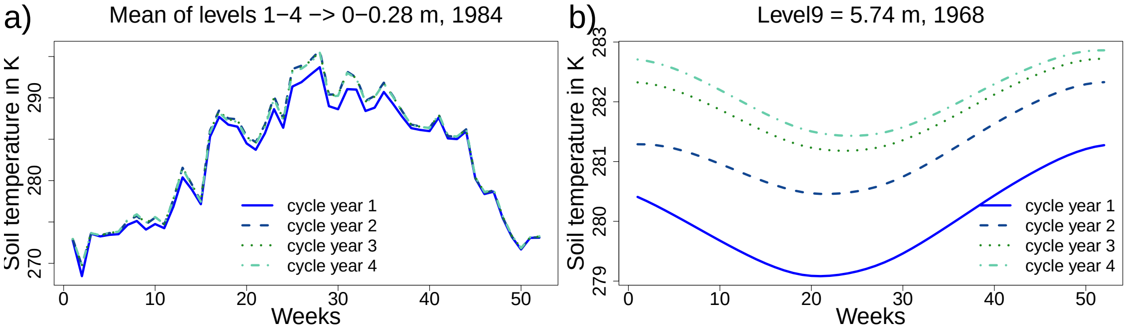

Figure 5.3: Weekly and areal mean of the soil temperature for the SMA in a cyclical stand-alone simulation of Veg3D, (a) mean of upper four levels, (b) ninth level

5.2 Cyclical Spin-Up with Veg3D

For the control run, a spin-up of the soil was performed by forcing Veg3D in the stand-alone mode with the atmospheric data of a former coupled run of the first simulation year 1968. The forcing data are provided by a coupled simulation of COSMO-CLM and TERRA_ML which is the standard SVAT-model coupled to COSMO. The horizontal grid spacing was 0.025 ° (approximately 2.8 km) as the final coupled simulations are performed on this grid. The stand-alone forcing was done cyclically for four years, so Veg3D was driven by the atmospheric data of 1968 four times in a row. Due to time issues, this was not conducted for the projection simulations. Still, all coupled simulations had a spin-up time of three years that were omitted from the data analysis (section 6.2).
Fig. 5.3 a reveals that in the upper layers, the soil temperature has mostly converged after the second cycle year. In the second lowest layer, on the other hand, there still is a decreasing difference between the soil temperature after three and four cycle years (Fig. 5.3 b).

5.3 Tests of Scenarios

5.3.1 Green Scenario

Several configurations of the vegetation parameters were tested to obtain the configuration for the green scenario. The setup of the domain and year is the same as in section 5.1.
As already described in section 3.3.3, reforestation as well as an increase in vegetated space and decreased energy consumption were assumed for the green scenario. For the parametrisation of these considerations, I tested the effects of a modification of several parameters. Fig. 5.4 presents the difference of soil temperature between the respective green scenario configuration and an unchanged configuration for LCZ 2 (a) and as a mean over all grid points (b), averaged over the upper four soil layers. The different configurations considered for the green scenario are:

- Doubling of maximum LAI (blue solid line): this would mean a change of the plant types. But it results in hardly any temperature change in the upper soil layers. Neither for land use class LCZ 2 (Fig. 5.4 a) nor for the average over all land use classes (Fig. 5.4 b).

- Decreasing the stomatal resistance r_{min} (light blue dashed line): this should result in elevated transpiration by the plants causing temperatures, but probably rather air temperatures than soil temperatures, to decrease. However, soil temperature differences are similarly small as for the increased maximum LAI.

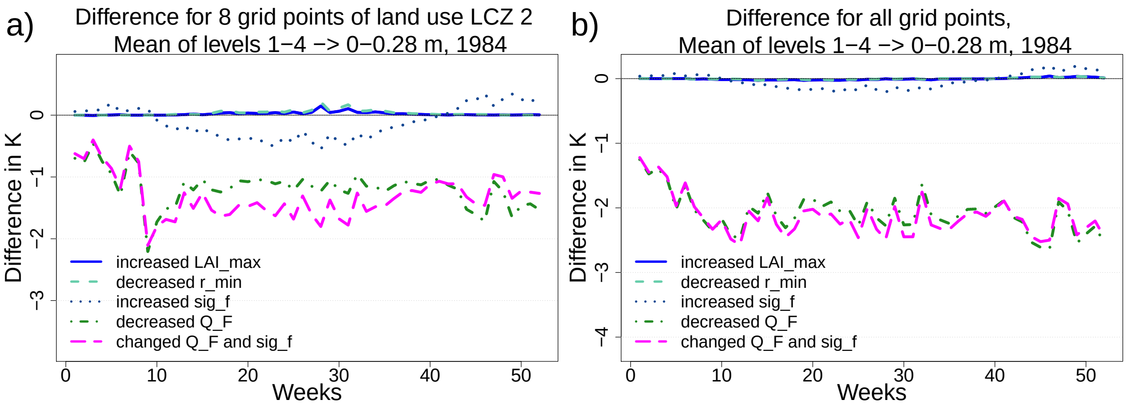

Figure 5.4: Difference of the weekly and areal mean of soil temperature of several green scenarios and the unchanged Veg3D (as used for reference and red scenario parametrisation), (a) land use LCZ 2, (b) all grid points; 1984

- Increasing the pervious surface fraction σ_f by 0.1 (blue dotted line) stands for a larger amount of vegetated surfaces, for example by planting grass onto roofs or greening parking spaces. This leads to a temperature decrease by up to 0.5 K in summer and a smaller increase by at the most 0.3 K in winter for LCZ 2. Averaged over the entire domain, the temperature difference lies in the range of $\pm$ 0.3 K.
- Decreasing Q_F by 40 % (dark green dashed and dotted line) causes the largest temperature change of single parameters. For LCZ 2, it results in a cooling by more than 1 K, averaged over the entire domain the cooling amounts to more than 2 K.
- The combination of increasing σ_f and decreasing Q_F (magenta dashed line) was the final setup for the green scenario. It results in a temperature decrease by about 1.5 K for LCZ 2 and nearly 2.5 K for the total domain.

With present climate change having caused an air temperature increase by about 1.2 K from 1931 to 2010 (section 3.2.1), mitigation strategies might even be able to completely diminish climate change in the near future.
I choose the combination of parameters that had the largest impact on soil temperatures to make sure to get a considerable change in the atmospheric variables for the coupled runs as well.

5.3.2 Red Scenario

As the red scenario differs from the reference only by a modified land use distribution (section 3.3.2), a change in soil temperature originates from an increased amount of urban grid points where anthropogenic heat is emitted. This results in an average temperature increase by about 1 K in the upper four soil layers (Fig. 5.5).

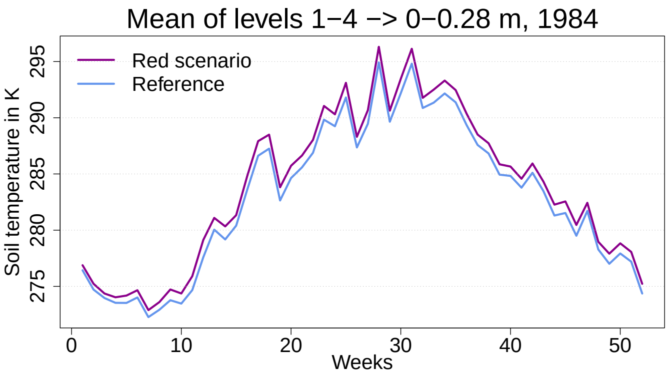

Figure 5.5: Weekly and areal mean of the soil temperature in the upper four layers for 1984, red scenario and reference land use distribution

6. Coupled Simulations COSMO-CLM and Veg3D

In this chapter, the coupled simulations are analysed and discussed. Before that I will describe the model configurations and time periods and also compare the simulations to observations.

6.1 Configurations and Time Periods

Two time periods are analysed in this thesis: the control period (1971-1975) and the projection period (2021-2025). At the beginning of my work, it was intended to simulate 30 years respectively, but several problems with the high performance computers and the model configuration prolonged the calculation time to such an extent that no more than these years could be simulated. Thus, the climate analysis is not as robust as when using 30 years as data basis: Fig. 6.1 displays the annual mean temperature of the analysis domain (see Fig. 6.2) taken from the HYRAS observational dataset (see section 6.3) and the respective average over five years, represented by the horizontal solid lines. The dashed line shows the mean over all 30 years. The variability of the five-year averages is

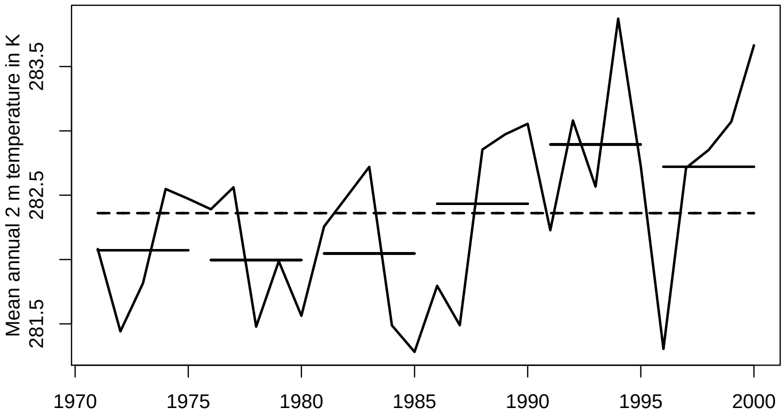

Figure 6.1: Annual mean 2 m temperature of HYRAS observational dataset, averaged over analysis domain as indicated by the white frame in Fig. 6.2. Five-year averages are plotted with solid lines, the dashed line represents the 30-year average.

very different: from 1971 to 1985 they do not change considerably, but from 1980 to 2000 the averages increase at first and finally decrease within the last decade. So a climate analysis conducted on five years can lead to significantly different results depending on the chosen time period. The variability is smaller when analysing longer time periods. Additionally, if trends within the time series from the control period to the projection period are not linear, the choice of the analysis periods has an influence on the evolving change signal. Comparing two periods of five years will probably result in a different change signal than when comparing two 30-year time periods.

The regional simulations were conducted on a horizontal grid spacing of 0.025 ° which corresponds to approximately 2.8 km. The simulation domain can be seen in Fig. 6.2. It encompasses large parts of Germany's southwest and west as well as eastern regions of France, Luxembourg and Belgium and a small part of northern Switzerland. For this thesis however, a domain of 8×8 grid points around the SMA is analysed. It is indicated by the white frame in Fig. 6.2. The land use distribution for the analysis domain was already presented in Fig. 3.8.

The COSMO-CLM version used is 4.8_clm19. The driving data are regional simulations with a grid spacing of 0.0625 ° (about 7 km) which were forced by ECHAM6 global simulations and provided by Katrin Sedlmeier. In view of the current emissions of greenhouse gases, the emission scenario RCP 8.5 was applied for the projection period.

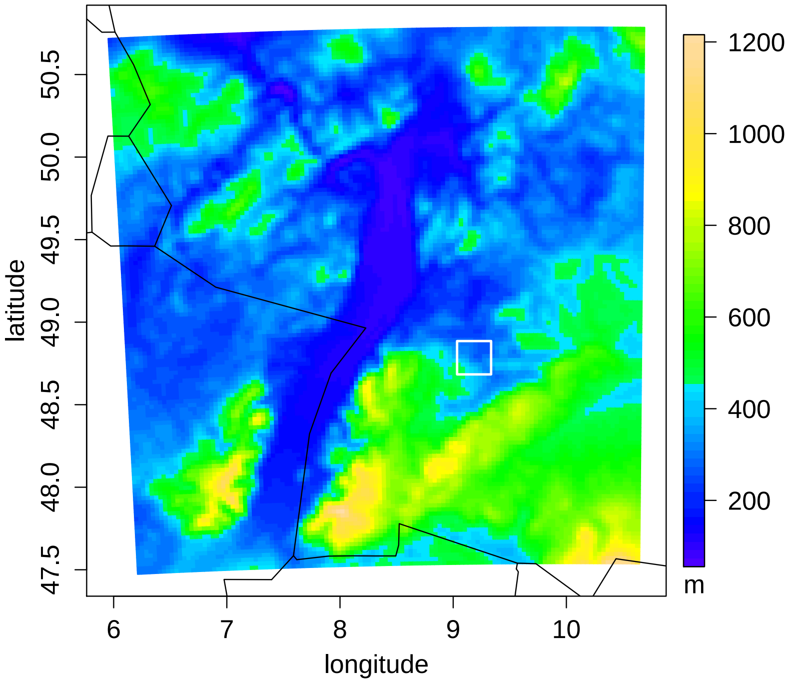

Figure 6.2: Topography of simulation domain with area of analysis indicated by white frame

To differentiate between the impact of climate change and the impact of land use alternations, projection simulations have been conducted with several scenarios (see also Fig. 1.1):

- same land use distribution and parametrisation as for control period to obtain the climate change signal (reference projection)
- red scenario characterised by a land use distribution with more densely built-up and industrialised areas (red scenario projection)
- green scenario with a reforested area in addition to smaller emissions of anthropogenic heat and more vegetated surfaces in urban land use classes (green scenario projection)

All projection simulations are driven by the same forcing dataset.
The control simulation and the red scenario projection were conducted on the high performance computer IC2 of KIT, both the green scenario and reference projection were run on the supercomputer Hornet of the High Performance Computing Center Stuttgart (HLRS).

6.2 Spin-Up and Initialisation

It takes some time for the climate in a model run to reach its equilibrium. Therefore, simulations are started some years before the actual evaluation period. The period that is not included in the analysis is called spin-up period. For this thesis, I applied a spin-up period of three years for the coupled system starting the control run in 1968 and the projection runs in 2018.
As we have already seen in section 5.2, the soil needs more time to reach its equilibrium than the atmosphere does. So the soil temperature and water content of the control run were initialised with fields that had been obtained by a cyclical four year stand-alone spin-up with Veg3D. Due to time issues, all projection runs were initialised with the soil temperature and water content provided by the forcing simulation.

6.3 Comparison to Observations

Some variables of the control run are compared to the observational dataset HYRAS (Rauthe et al., 2000). It provides gridded daily values for temperature on a 1 km-grid and for precipitation on a 5 km-grid covering major parts of Central Europe. The data basis are measurements at stations. To be comparable to the simulation, HYRAS data were interpolated onto the model's 2.8 km-grid. Additionally, the region that will be analysed in the following sections is indicated by a black frame in Fig. 6.3 and 6.4.

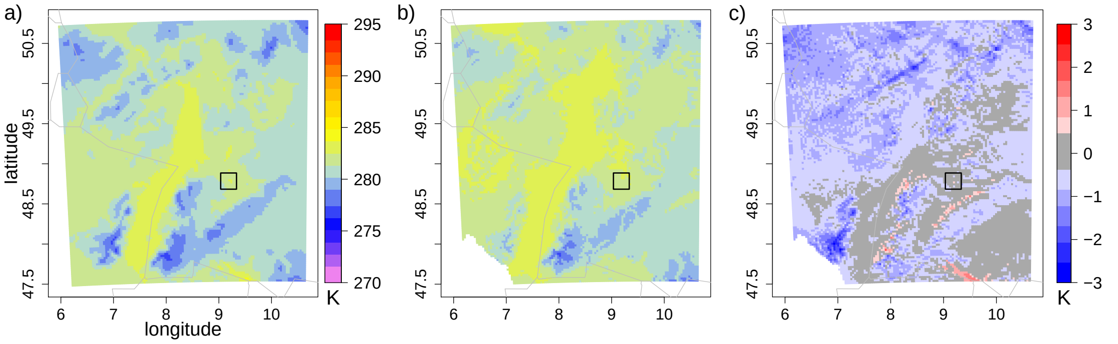

Figure 6.3: Mean of 2 m temperature, 1971-1975 of (a) control simulation and (b) HYRAS observation, (c) difference between simulation and observation

6.3.1 Temperature

Simulated average 2 m temperatures are mostly lower than observed ones or within a range of ± 0.4 K difference (Fig. 6.3 c). The largest temperature differences occur mainly in elevated regions apart from the Black Forest and Swabian Jura.

But with a Root Mean Square Error (RMSE) of 0.77 K over the entire domain, modelled temperature does not differ too much from the observations. In the area of the SMA, which is analysed later, hardly differences larger than 0.4 K occur.

6.3.2 Precipitation

Clearly, CLM overestimates yearly total precipitation sums (Fig. 6.4 c). Especially in mountainous terrain like the Vosges and the Black Forest, mean yearly sums of the simulation are about 2000 mm larger than those of the observations. Apparently, this overestimation in higher elevations is a problem of high-resolution simulations with CLM as the overestimation is not that large for 7 km simulations (Hackenbruch, 2015). The bias might occur due to boundary effects which will soon be tested in the working group by enlarging the simulation domain. But again, in the region of analysis there is a relatively small precipitation bias.

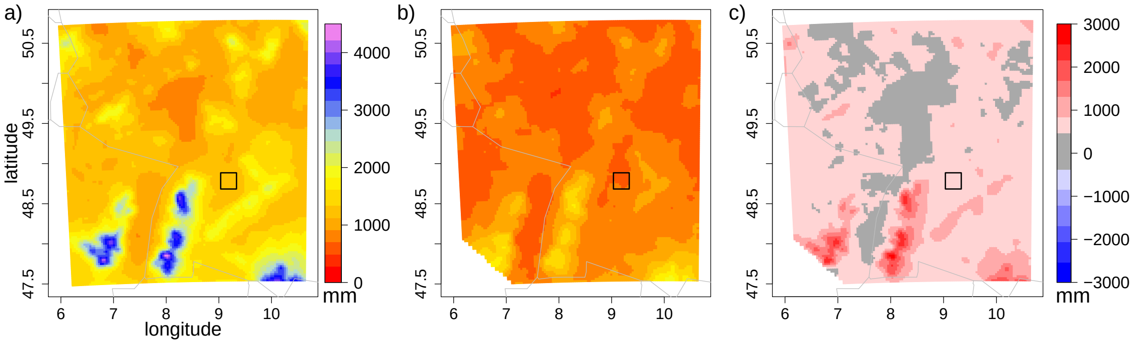

Figure 6.4: Mean of yearly precipitation sum, 1971-1975 of (a) control simulation and (b) HYRAS observation, (c) difference between simulation and observation

However, as the aim of this thesis is the quantification of the impact of climate change and land use on future climate, the differences between the simulations are analysed. So biases of the model do not have an impact on the results as they are assumed to occur for both the control and projection period.

6.4 Climate Change Signal

The following sections present the results of the different coupled simulations. Apart from the analysis of frost days, which is performed for the winter months of November through April, I will focus on the summer months of May through October. The most relevant changes are expected for this season as especially in summer, the meteorological situation can have major impacts on city dwellers. For example, an additional rise of temperature due to urban land use change increases the heat stress during summer in cities. During winter on the other hand, the impact of a temperature increase due to climate change or land use change is favourable because both human health and infrastructure benefit from milder winter conditions.

In sections 6.4 to 6.6, most of the results are presented as an average of summer means or summer sums on a map to be able to relate land use to the evolving pattern. Positive deviances of the compared simulations are indicated by red colours, negative deviances by blue colours. Additionally, a χ^2-homogeneity test was applied on the daily probability density functions of each grid point to assess the significance of the differences on a 95 %-level. Grid points with a significant change are marked by circles in the maps.
In this section, a comparison of the control run and the reference projection is presented to show the influence of climate change on future urban climate in the SMA. I will also try to assess the influence of the urban land use parametrisation on the variables. Grid points marked with crosses in the maps indicate urban land use. Figures that are not shown here are listed in appendix A.2.
It is followed by sections 6.5 and 6.6 analysing the red scenario and green scenario, respectively. Section 6.7 finally rates the different impacts of climate change and land use change in the city centre of Stuttgart.

6.4.1 Temperature

Mean Summer Temperature

Generally, the spatial distribution of the average 2 m temperature during summer (Fig. 6.5 a and b) exhibits lowest values in higher elevated regions of the domain's southwest and highest values in lower elevations in agreement with the height-dependence of temperature.
The temperature difference between the control time period and the projection period ranges from +0.65 to +0.9 K and is significant for several grid points(Fig. 6.5 c). At grid

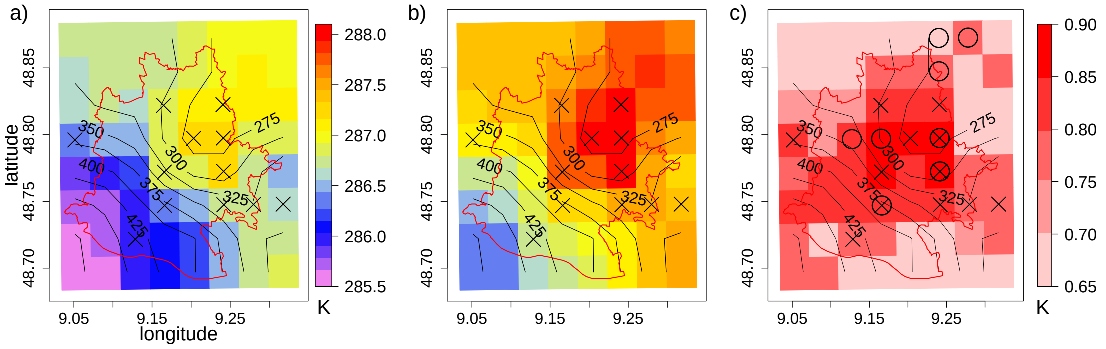

Figure 6.5: Mean summer 2 m temperature of first five analysis years, (a) control run 1971-1975, (b) reference projection 2021-2025, (c) difference between projection and control run. Circles mark significant differences on a 95 %-level, crosses indicate urban land use, black lines show the height of the terrain and the area of Stuttgart is indicated by the red polygon.

points with an urban land use class, the temperature increase is largest due to the lower amount of pervious surfaces (see Tab. 4.1) preventing evaporational cooling.

The probability density function of the hourly mean 2 m temperature exhibits a parallel shift to the right when comparing the reference projection to the control run, increasing the mean by 0.75 K (Fig. 6.6). The standard deviation decreases slightly from 4.79 to 4.72 K. This implies that climate change has a larger influence on the mean temperature than on extremes during summer as the density function shifts to the right but hardly changes its shape. The change in hourly 2 m temperature is significant on a 95 %-level.

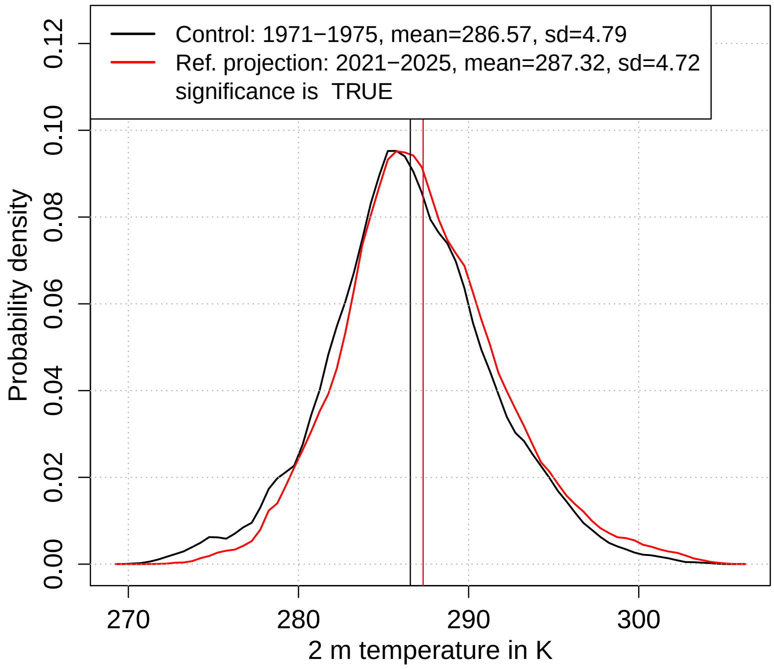

Figure 6.6: Probability density functions of the hourly mean temperature during summer for the control period (1971-1975, red) and the reference projection (2021-2025, red)

The observed summer temperature increase by 1 K from 1931 to 2010 (section 3.2.1) which corresponds to approximately 0.13 K per decade is a bit larger than the overall summer temperature increase per decade of the simulations which amounts to about 0.09 K.

Summer Days

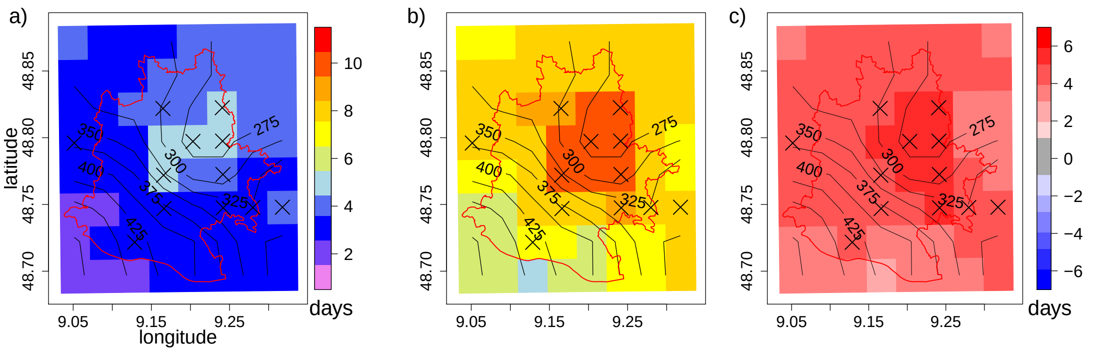

Figure 6.7: Same as Fig. 6.5, but for mean annual number of summer days ($T_{max} \geq 25\,^\circ$ C)

As can be expected, the mean annual number of summer days (days with $T_{max} \geq 25\,^\circ$ C) increases as well (Fig. 6.7 c). The difference lies between three and six days for the SMA. The highest increases in the number of summer days occur at grid points with urban land use.

The significance of the difference could not be tested as the distributions of each grid point only consist of five values (one per year) which is not sufficient for the χ^2-homogeneity test.

Comparing the numbers of summer days of the control run to that presented in section 3.2.1, the simulation shows considerably less summer days than observed during the period 1971-2000. The shorter amount of time analysed might be one reason for this, as one exceptional year can have a large impact on the mean of the time period. Additionally, 1971-1975 are the first years of the 30-year period, so they can be presumed to be the coldest years of the 30-year period leading to a smaller number of summer days for the period 1971-1975 compared to 1971-2000. For the observations, the mean temperature of the period 1971-1975 is lower than that towards the end of the century (Fig. 6.1).

Frost Days

The spatial distribution of the difference of the mean number of frost days (daily minimum 2 m temperature $T_{min} < 0\,^\circ$C, Fig. 6.8) shows an interesting feature that was not expected at first: in the reference projection, more frost days occur than in the control simulation. The differences are smallest at higher elevations and the largest differences occur at rural grid points. So urban land use seems to reduce the general increase in the

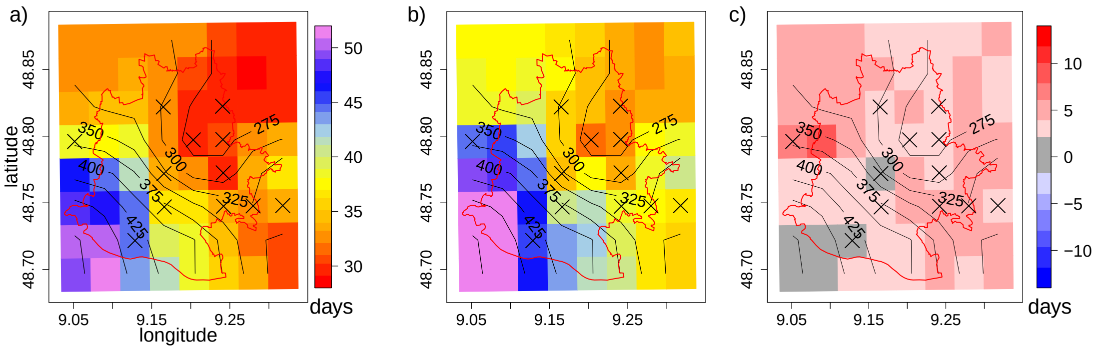

Figure 6.8: Same as Fig. 6.5, but for mean annual number of frost days ($T_{min} < 0\,^{\circ}$ C)

number of frost days.

The rise of the number of frost days by up to nine days again portrays the problem of a climate analysis based on five years (leaving only four complete winters to look at). Fig. 6.9 shows that for the respective second and third winter the spatially averaged number of frost days is larger for the projection (red) than for the control run (black).

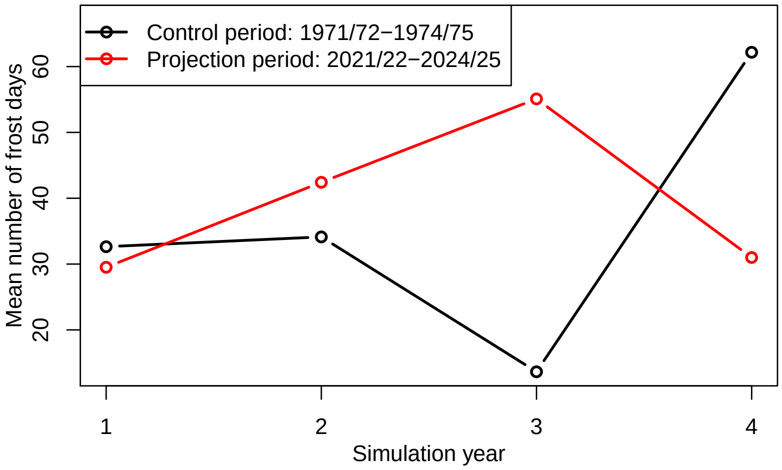

Figure 6.9: Mean number of frost days averaged over analysis domain for the control period (1971-1975, red) and the reference projection (2021-2025, red)

6.4.2 Precipitation

Summer Precipitation Sum

The average summer precipitation sum of the reference projection is larger than that of the control simulation in the entire domain. The maximum difference amounts to 60 mm (Fig. 6.10 c). The majority of the pronounced changes occurs along the slopes of the Filder in the southwestern centre of the domain. But none of the changes in precipitation are significant (when looking at daily sums of precipitation), so the increase might only depict the noise caused by the short averaging period. It can only be stated that there

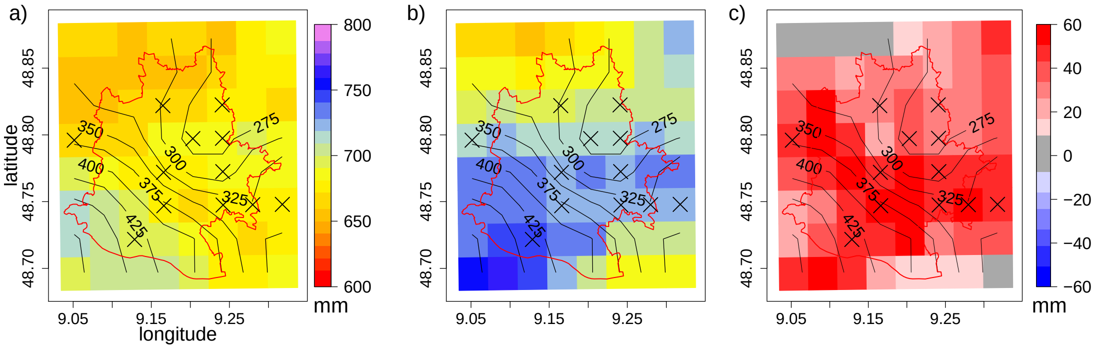

Figure 6.10: Same as Fig. 6.5, but for mean summer precipitation sum

is a tendency of more precipitation in future summers. As precipitation is influenced by many processes as well as large-scale weather patterns, it is difficult to relate changes in precipitation and land use parametrisation.

Generally, the spatial distribution is more variable in the projection than in the control period (Fig. 6.10 a and b) as the maximum precipitation amounts at the higher elevations in the southwest increase by larger amounts than in the northwest where the minimum sum of precipitation occurs.

Extreme Precipitation

As a measure of extreme precipitation, I counted the days per grid point at which the daily sum of precipitation amounted to at least 20 mm (Fig. 6.11). In about one third of the domain, two or three more days with extreme precipitation occur in the reference future than in the control run corresponding to a relative increase by about 25 to 40 %. Just as for the total sum of summer precipitation (Fig. 6.10 c), these grid points mostly lie along the slopes of the Filder. One reason for the increase in extreme precipitation might be local thunderstorms developing independently from large-scale weather patterns. However, the mean summer sum of CAPE decreases by small amounts in the entire analysis domain (not shown).

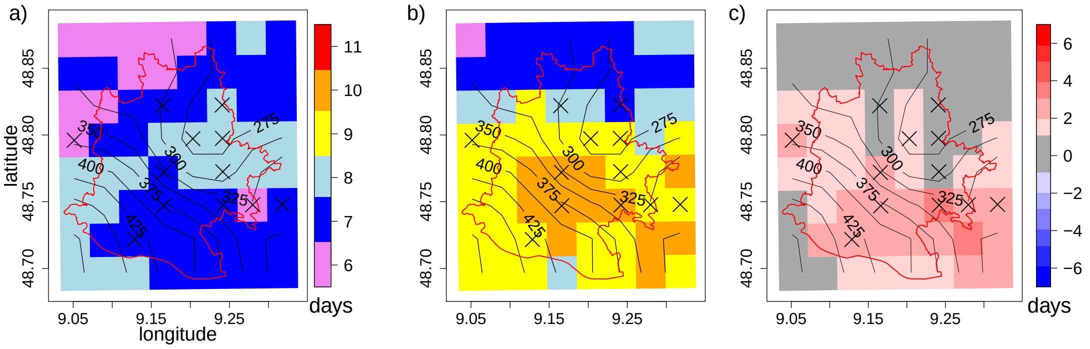

Figure 6.11: Same as Fig. 6.5, but for mean annual number of summer daily sum of precipitation $\geq$ 20 mm

The probability density function of daily precipitation sums also shows that extreme daily precipitation increases in future as the tail of the function is shifted to the right by nearly 20 mm and generally, high precipitation days occur more frequently (Fig. 6.12). According to the χ^2-homogeneity test, the changes are significant. But again, the probabilities for extreme daily precipitation are small and might only be caused by noise.

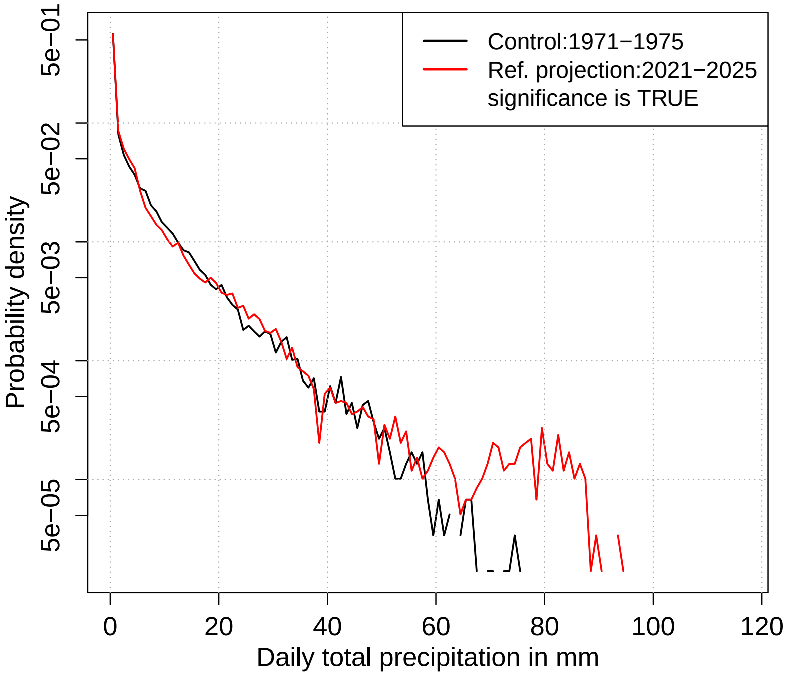

Figure 6.12: Probability density functions of the daily sum of precipitation during summer. Black indicates the control period (1971-1975), red marks the reference projection (2021-2025).

6.4.3 Wind Direction

The probability density distribution of the hourly meteorological wind direction at 10 m for the day (8:00 - 19:00) during summer shows the large peak for southwesterly and westerly directions caused by large-scale atmospheric flow and the channelling through the Nesenbach valley which increases for the reference projection (Fig. 6.13 a). The secondary maximum of the control run at southeasterly directions following the Neckar valley, however, disappears for the projection. Detailed analysis of the data showed no relation of the easterly wind directions to specific years or grid points. A possible explanation for the decrease of the easterly peak might be a small shift in the main direction of the atmospheric flow. If it is mostly perpendicular to the Neckar valley, even a slight shift causes the wind to be channelled either in southeastern or northwestern direction. As western wind directions become more frequent in future, the channelling in the southeastern direction occurs less often. This can be seen from Fig. 6.13 a, since the area between the two curves for the control run's secondary peak at 100 ° and the westerly

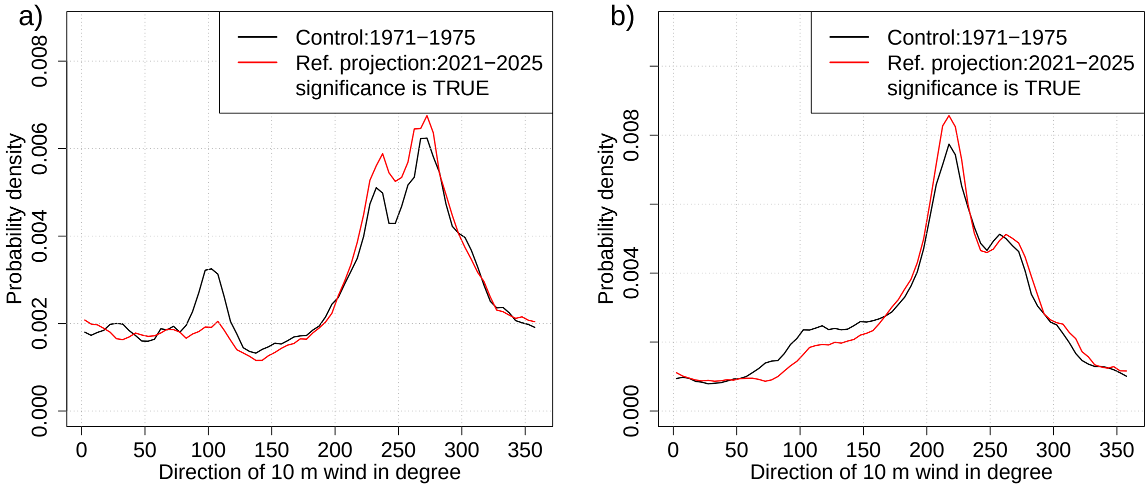

Figure 6.13: Probability density functions of direction of 10 m wind in summer during the day (8:00 - 19:00, a) and during the night (20:00-7:00, b) for the control period (1971-1975, red) and the reference projection (2021-2025, red)

directions is approximately the same. The change of the wind direction is significant on a level of 95 %.

During the night (20:00 - 7:00, Fig. 6.13 b), the peak at southwesterly directions increases and more (north)westerly winds occur. Fewer easterly winds evolve as well and the change is significant, just like during day hours.

6.4.4 Global Radiation, Total Cloud Cover and Specific Humidity

In future, days with little solar global radiation (sum of diffuse and direct downward solar radiation at the surface) of up to 2.5 kWh/m^2 and days with 7 to 8 kWh/m^2 will become more frequent in the SMA (Fig. 6.14). On the other hand, days with medium irradiation of about 4 to 7 kWh/m^2 will occur less often compared to the control period. This change is significant on a level of 95 %.

Looking at the spatial distributions of the mean summer sum of global radiation, the decreases in the future range from 40 to 15 kWh/m^2 (Fig. 6.15 c). They are significant for nearly one third of the domain when looking at daily sums of global radiation, but still the mean change is very small again.

Global radiation is dependent on cloud cover and humidity in the boundary layer as both clouds and water vapour attenuate direct solar radiation. So a combination of the spatial distributions of total cloud cover (Fig. 6.16 a and b) and 2 m specific humidity (Fig. 6.17 a and b) helps to explain the evolving large-scale pattern of global radiation (Fig. 6.15 a and b): both in the control period and the reference projection, cloud cover is lower in the western part of the SMA. Minimum humidity occurs in the southwestern part of the domain. Thus, maximum global radiation occurs in the southwest decreasing slightly to the northwest and the minimum evolves in the northeastern part of the domain.

An interesting feature of the spatial distributions of global radiation of both the control

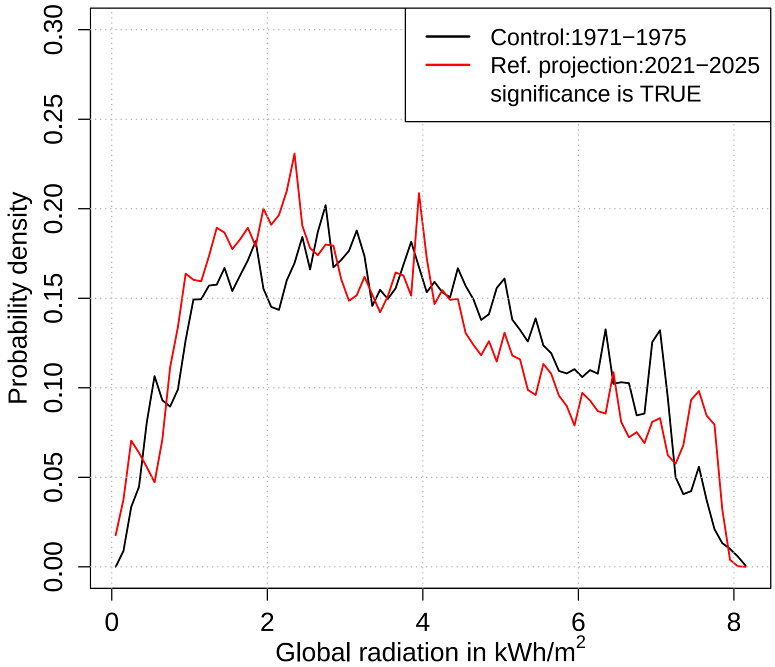

Figure 6.14: Probability density functions of the daily sum of global radiation for the control period (1971-1975, red) and the reference projection (2021-2025, red)

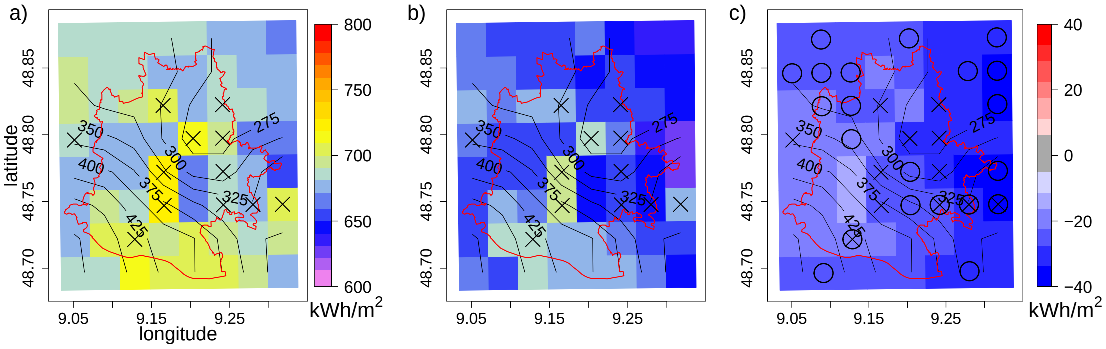

Figure 6.15: Same as Fig. 6.5, but for mean summer sum of global radiation

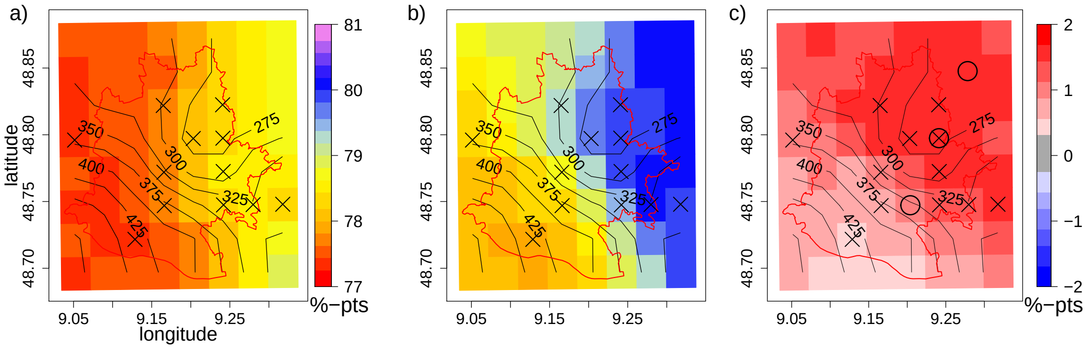

Figure 6.16: Same as Fig. 6.5, but for mean summer total cloud cover

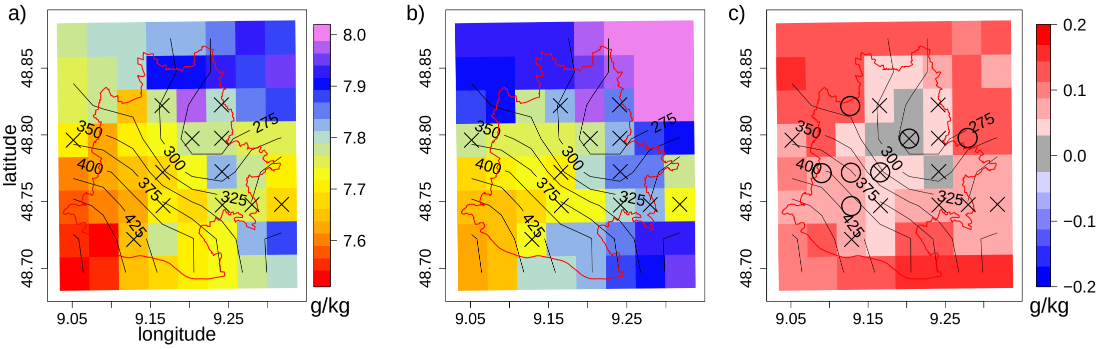

Figure 6.17: Same as Fig. 6.5, but for mean summer 2 m specific humidity

and reference simulation is that especially at western urban grid points the radiation is higher than at rural grid points by up to about 50 kWh/m^2. The grid points with the highest summer sum of global radiation belong to three different urban land use classes (Fig. 3.8), so urban land use generally seems to cause global radiation to increase here. One possible mechanism for the connection of global radiation and land use is the following: The fraction of pervious surfaces for urban land use classes is considerably smaller compared to rural classes (Tab. 4.1). Thus, less soil humidity is available for evapotranspiration into the atmosphere and humidity is lower near urban grid points. This should lead to higher values of global radiation either directly through less attenuation by water vapour or through the formation of fewer clouds.
But neither the spatial distribution of total cloud cover nor of 2 m specific humidity show a connection to urban land use as distinct as global radiation (Fig. 6.16 and Fig. 6.17 a and b, respectively).
Another reason for elevated global radiation at the ground might be a change in cloud properties or vertical cloud distribution leading to an increase in direct solar radiation.

The changes of 2 m specific humidity from the control period to the projection period are small (Fig. 6.17 c), but still exhibit a pattern that suggests a physical explanation. The largest increases in humidity occur close to the border of the domain where rural land use prevails. As the fraction of vegetated surfaces is larger here than at urban grid points, evapotranspiration also is larger and more dependent on precipitation and soil moisture. Thus, the small growth of total summertime precipitation (Fig. 6.10 c) might lead to an increase in humidity in rural areas, but not in urban areas. The overall rise of temperature also has a larger effect on humidity for rural land use than for urban land use, since generally less soil moisture is available in cities due to the large amount of impervious surfaces. So an increase in temperature leads to a higher amount of evapotranspiration, and thus specific humidity, at rural land use classes.

Total cloud cover increases in the entire domain from the control period to the projection period (Fig. 6.16 c). These changes are very small again (not more than 3 % relatively), but significant for several grid points when looking at the daily mean cloud cover. The strongest increases occur in the northeast of the domain. The larger amount of total cloud cover probably results from the additional humidity as described above. But as the process chain from evaporation to condensation and cloud formation is long and also influenced by advection, no connection of cloud cover change and land use evolves.

6.4.5 Summary Climate Change Signal

The mean summer 2 m temperature increases by 0.65 to 0.9 K in the analysis domain. The increase is significant for several grid points. The mean number of summer days grows as well, by three to six days per summer. Unexpectedly, the number of frost days in the future is also greater than in the control period. Up to nine more frost days occur in the reference projection, mostly the increase amounts to four or five additional frost days. The mean sum of summer precipitation grows slightly by up to additional 60 mm. In about one third of the domain, more days with extreme precipitation occur, the increase is up to 40 %. The secondary peak of the probability density function of the 10 m wind direction during the day at 100 ° disappears for the reference projection. The summer sum of global radiation decreases significantly by up to 40 kWh/m^2. For summer 2 m specific humidity, a small increase above rural areas can be seen. Total cloud cover increases by small amounts during summer as well. However, most of the changes are small and for the reasons described in section 6.1 allow only an estimation of the tendencies of the variables.

6.5 Influence of Urban Planning Scenarios - Red Scenario

This section presents the results of the coupled simulation of the red scenario projection compared to the reference projection. As a reminder: for the red scenario, more grid points are assigned urban land use classes and most grid points that are covered by urban land use in the reference already, change to a more densified settlement or industrial land cover. I will refer to these grid points as 'intensified grid points' and they are marked by crosses on the maps.

Only maps of the differences of the red scenario and reference projection are shown in this section. The absolute values and variables not presented here are provided in appendix A.2.

6.5.1 Temperature

Mean Summer Temperature and Summer Days

When looking at the spatial distribution of summer 2 m temperature (Fig. 6.18), one grid point in the red scenario projection stands out especially with a temperature difference of more than 1.3 K which is the only significant change of the domain. This grid point is

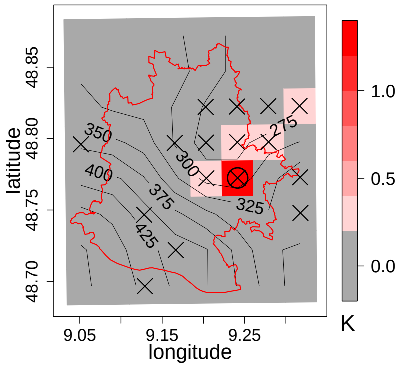

Figure 6.18: Mean summer 2 m temperature 2021-2025, difference between red scenario and reference projection. Circles mark significant differences on a 95 %-level, crosses indicate intensified grid points, black lines show the height of the terrain and the area of Stuttgart is indicated by the red polygon.

assigned land use class LCZ 10 with an anthropogenic heat input Q_F of 300 W/m^2 in the red scenario projection. It will be prominent in many of the analysed variables, so I will refer to it as 'LCZ 10-grid point' from now on.

Generally, considerable temperature increases only occur at intensified grid points. However, at some intensified grid points, the rise in temperature lies in the range of grid points without a change in land cover. So the larger increase in temperature of the three grid points neighbouring the LCZ 10-grid point might be partly caused by advection of the high amount of Q_F, an effect which can only be produced by a coupled simulation.

The mean number of summer days (not shown) shows a similar pattern of differences as 2 m summer temperature, with the largest increase by five days at the LCZ 10-grid point and five additional intensified grid points with an increase larger than one day.

Frost Days

Also when analysing the mean number of frost days per winter (Fig. 6.19), the LCZ 10-grid point displays the maximum decrease in the number of frost days. Two intensified grid points that are not in direct proximity to the LCZ 10-grid point show differences to the reference projection, so not only the Q_F of 300 W/m^2 and its advection cause the number of frost days to decrease.

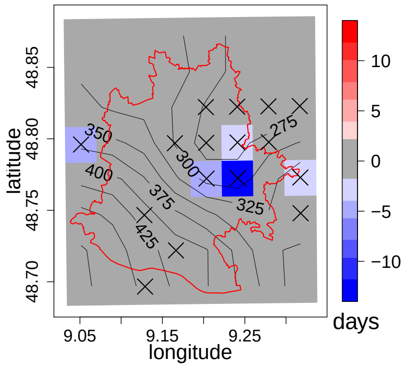

Figure 6.19: Same as Fig. 6.18, but for mean annual number of frost days ($T_{min} < 0^\circ$ C)

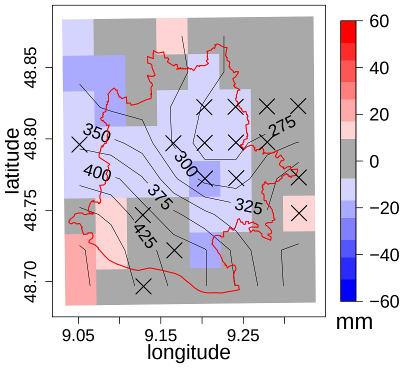

Figure 6.20: Same as Fig. 6.18, but for mean summer precipitation sum

6.5.2 Precipitation and Total Cloud Cover

The total amount of summer precipitation (Fig. 6.20) decreases slightly in about one third of the domain. Extreme daily precipitation shows no differences by more than one day either (not shown). Total cloud cover shows the largest difference at the LCZ 10-grid point, but the difference still is not larger than 0.4 percentage points (not shown). As the changes are so small, it is difficult to asses their practical relevance.

6.5.3 Vertical Wind and CAPE

The vertical wind is shown only for the red scenario as only for this simulation a significant and interesting change occurs. The level of the vertical wind analysed here is the model level 33 which corresponds to a height above ground level between 525 m at the high elevations and 533 m at lower elevations in the SMA.

The spatial distributions of the mean summer vertical wind speed during the day (8:00 - 19:00) display a connection to topography (Fig. 6.21 a and b): in higher elevations to the southwest there is subsidence, in lower elevations to the east ascension prevails.

The only significant changes in mean summer vertical wind occur at the LCZ 10-grid point

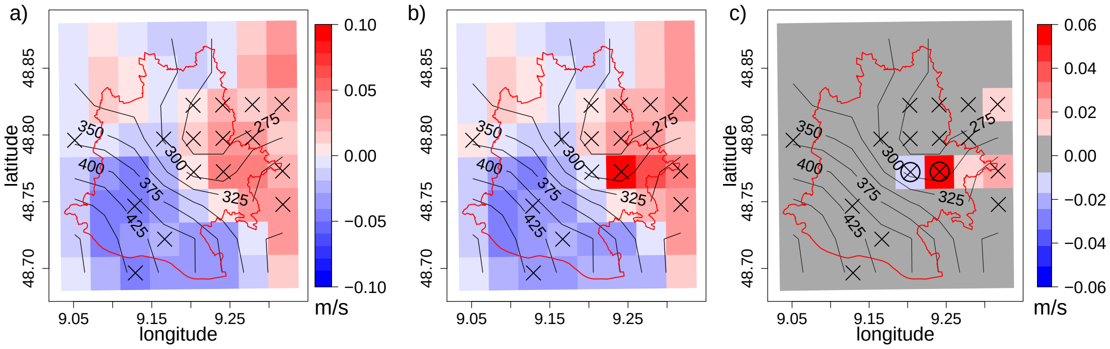

Figure 6.21: Mean vertical wind speed during summer at appr. 530 m above ground during the day (8:00 - 19:00) 2021-2025, (a) reference projection, (b) red scenario projection, (c) difference between red scenario and reference projection. Circles mark significant differences on a 95 %-level, crosses indicate intensified grid points, black lines show the height of the terrain and the area of Stuttgart is indicated by the red polygon.

where it increases by about 0.05 m/s and its neighbouring grid point to the west where the vertical wind decreases and changes from ascending to descending (Fig. 6.21 c). This means that the additional amount of Q_F triggers convection above the LCZ10-grid point (as was anticipated before in section 4.3.2) similar to the urban breeze mentioned in section 2.1. The large increase in CAPE above this grid point confirms this (Fig. 6.22 c). Additionally, the amount of the horizontal 10 m wind during the day increases significantly at the LCZ 10-grid point and four of its eight neighbouring grid cells (not shown). This illustrates the low-level convergence induced by the urban breeze.

Parts of the descending branch of the circulation are situated above the grid point to the west of the LCZ 10-grid point. At its eastern grid point, the vertical wind grows even though no intensification occurs here. As the main horizontal wind direction is southwest to west, some of the 300 W/m^2 or the ascension itself might be advected to this eastern grid cell causing more updrafts here as well.

When looking at the vertical wind during the night (not shown), more ascension occurs above the LCZ 10-grid point as well. However, at its neighbouring western grid cell, the average ascension only is reduced, not turned into subsidence.

The fact that intensification has an influence on vertical wind speed, but not on precipitation and only a small influence on total cloud cover leads to the assumption that the additional Q_F causes dry convection by generally raising the sensible rather than the latent heat flux. This partitioning evolves because for urban land use, the fraction of surface covered by vegetation is significantly smaller than for rural land use (Tab. 4.1). Thus, a much smaller amount of soil humidity is available to the atmosphere causing limited emissions of latent heat.

Additionally, Fig. 6.21 shows the vertical wind speed at a height of approximately 530 m above ground. During the day, this mostly is inside the atmospheric boundary layer. So the urban breeze caused by the 300 W/m^2 probably only exists within the boundary layer and has no direct effect on the free atmosphere.

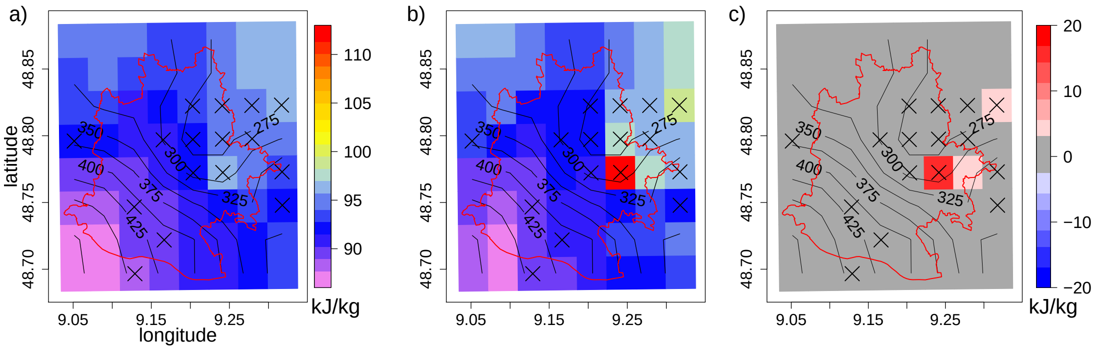

Figure 6.22: Same as Fig. 6.21, but for mean summer sum of CAPE

6.5.4 Global Radiation and Specific Humidity

The impact of the red scenario on global radiation is not very large (Fig. 6.23). The maximum amounts of changes are up to ± 30 kWh/m^2. Nevertheless, the downward radiation decreases above the LCZ 10-grid point and its neighbouring grid point to the east whereas radiation increases above its western neighbouring grid point. This probably depicts the small impact of the 300 W/m^2 on cloud cover and its advection to the east again. The largest decreases in global radiation occur at the two grid points where Q_F increased by the largest amounts.

At those grid points where global radiation increases, land use changed from a rural to an urban land use class. The connection to irradiation might be via less evaporation through the increased amount of impervious surfaces leading to lower integrated amount of water vapour in the boundary layer as described in detail in section 6.4.4. The distribution of the changes of 2 m specific humidity confirms this assumption for some of these grid points where humidity decreases (Fig. 6.24).

Again I have to emphasise on the small amount of the occurring differences and the difficulty of relating them to physical explanations.

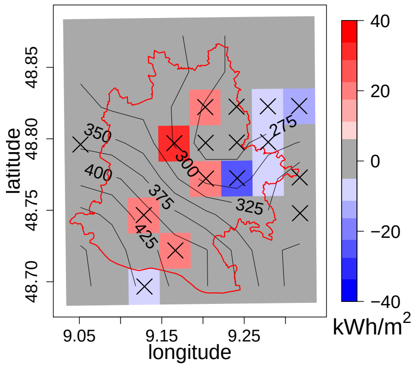

Figure 6.23: Same as Fig. 6.18, but for mean summer sum of global radiation

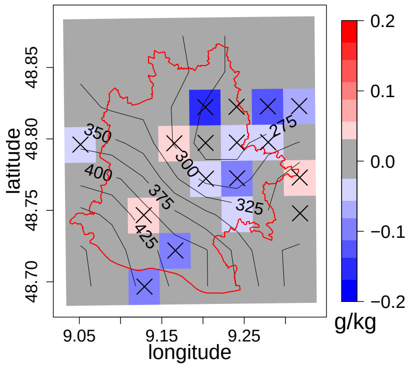

Figure 6.24: Same as Fig. 6.18, but for mean summer 2 m specific humidity

6.5.5 Summary Red Scenario Projection

At some intensified grid points, summer 2 m temperature increases by approximately 0.4 K, but at that grid point where Q_F rose to 300 W/m^2, temperature increases significantly by more than 1.3 K. It is also here, where the number of summer days increases or the number of frost days decreases most, respectively. Hardly any changes of precipitation occur, neither for the mean summer sum, nor the number of extreme daily precipitation. Total cloud cover shows no large differences as well. Looking at mean summer vertical wind speed during the day suggests that the anthropogenic heat input of 300 W/m^2 trigger an urban breeze with significantly more ascension above this grid point and a significant change from ascension to subsidence above its western grid point. CAPE also increases by a large amount at the LZC 10-grid point. Global radiation shows small decreases and increases with a maximum range of $\pm$ 30 kWh/m^2 mostly at intensified grid points.

The only significant changes compared to the reference projection occur at the LCZ 10-grid point for 2 m mean summer temperature and the vertical wind, and at its neighbouring grid cell to the west for the vertical wind. The changes of the other variables are mostly restricted to intensified grid points and smaller than those caused by climate change. Some of them are so small that they would hardly be detectable in observations. This analysis bases only on one model realisation, so it is possible that for another realisation, e.g. a different forcing dataset, the differences caused by land use modifications would be larger. Thus, ensemble simulations would be useful to assess the spread and uncertainties of the land use scenarios.

6.6 Influence of Urban Planning Scenarios - Green Scenario

In this section, the simulation results of the green scenario projection are compared to the reference projection. For the green scenario, the distribution of land use classes changed only at eight southern grid cells from agriculture to mixed forest simulating reforestation. These grid points are indicated by squares in the maps. Additionally, Q_F of the urban land use classes was reduced by 40 % and the fraction of vegetated surfaces at urban grid points was increased by 10 percentage points. I will refer to this measure of changing the urban land use parameters as 'mitigation' from now on. Crosses again indicate urban land use.

Only maps of the differences of the green scenario and reference projection are presented in this section as well. The absolute values can be seen in appendix A.2.

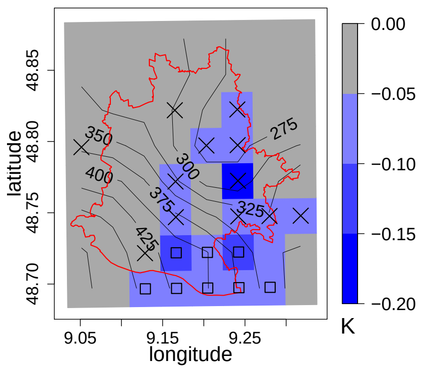

Figure 6.25: Mean summer 2 m temperature 2021-2025, difference between green scenario and reference projection. Circles would mark significant differences on a 95 %-level, crosses indicate urban land use, squares indicate reforestation, black lines show the height of the terrain and the area of Stuttgart is indicated by the red polygon.

6.6.1 Temperature

Mean Summer Temperature and Summer Days

For the green scenario projection, mean summer 2 m temperature decreases by small amounts for several grid points compared to the reference projection (Fig. 6.25). Maximum cooling is up to 0.2 K. Reforestation has nearly the same influence on 2 m temperature as mitigation, since all eight grid points now covered by mixed forest show a temperature decrease by more than 0.05 K. However, none of the differences are significant and the amounts are very small.

The mean number of summer days changes by not more than one day (not shown).

Frost Days

The mean annual number of frost days increases by at least two days for one quarter of the domain (Fig. 6.26). The largest increases occur at those grid cells where land use changed from agriculture to mixed forest. Actually, one would expect fewer cold temperatures to occur in reforested areas as forest buffers extreme temperatures more than agriculture does.

All in all, reforestation has a larger impact on low temperatures than mitigation does. Even though the changes are not large, some of them are in the order of magnitude of

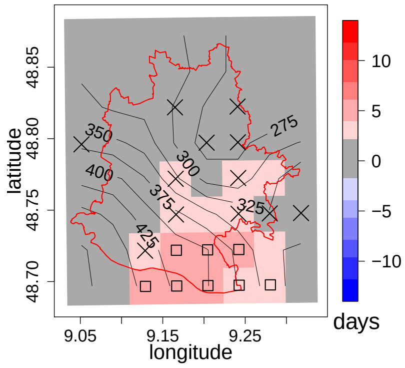

Figure 6.26: Same as Fig. 6.25, but for mean annual number of frost days ($T_{min} < 0\,^{\circ}$ C)

the climate change signal (Fig. 6.8).

6.6.2 Precipitation

In the green scenario, the mean number of extreme daily precipitation changes by not more than one day and only very small changes of the summer sum of precipitation occur (Fig. 6.27). Most of the changes are negative and they are largest in the centre of the domain where many urban grid points are located. So the decrease in Q_F might lead to slightly reduced convection resulting in less precipitation. Fig. 6.30 does show small decreases in CAPE above two mitigated grid points, but also above reforested grid points where small increases in precipitation occurs. But as the changes of precipitation are so small, they would probably lie in the range of noise of ensemble simulations.

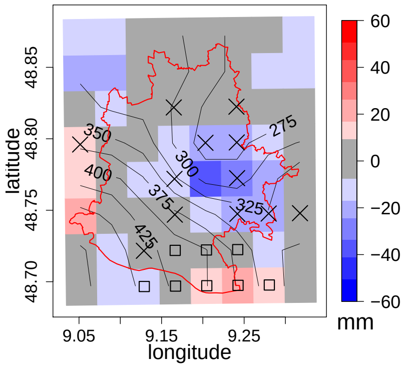

Figure 6.27: Same as Fig. 6.25, but for mean summer precipitation sum

6.6.3 Global Radiation and Total Cloud Cover

Global radiation does not change at mitigated grid points, but at all but one of the grid points that were reforested where it decreases by more than 10 kWh/m^2(Fig. 6.28). This is a very small change, but it is interesting that reforestation has an influence on solar radiation, in contrast to mitigation. At some of the reforested grid points, the total cloud cover increases by small amounts (not shown) which probably is one reason for less downward radiation reaching the ground.

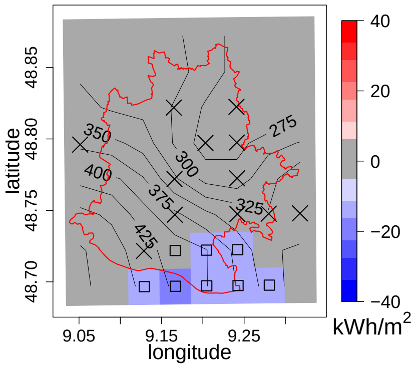

Figure 6.28: Same as Fig. 6.25, but for mean summer sum of global radiation

6.6.4 Specific Humidity and CAPE

Only reforestation has an influence on mean summer specific humidity about the same order of magnitude as climate change (Fig. 6.29). At those grid points, humidity decreases by small amounts. In the lowest two model layers though (up to a height of nearly 50 m, not shown), no change in humidity occurs. This seems to contradict the assumption drawn in section 6.4.4 on the connection between less humidity leading to more global radiation. One aspect to be considered when looking at specific humidity is that the sources for transpiration lie in lower soil layers for forest than for agricultural plants. So the distributions of soil humidity and precipitation also have an influence on the differential amounts of transpiration by either forest or agricultural plants and might lead to the decrease in 2 m specific humidity.
The decrease in specific humidity probably is the reason for the decreasing summer sums of CAPE at the reforested grid points (Fig. 6.30) as it depends on virtual temperature. The only two mitigated grid points with a decrease in CAPE exceeding 1 kJ/kg are those with the largest absolute decrease in Q_F. So the reason for lowered CAPE at the reforested area might be decreased humidity and at the urban grid points, probably the decrease in Q_F leads to the smaller amount of CAPE. But again, the changes are small and could probably not be detected in nature.

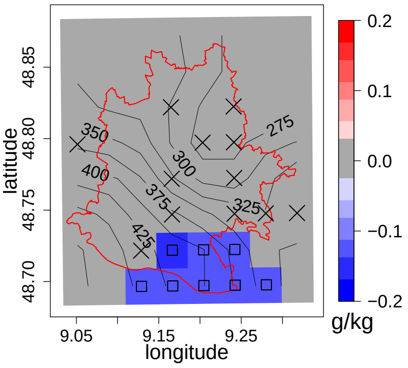

Figure 6.29: Same as Fig. 6.25, but for mean summer 2 m specific humidity

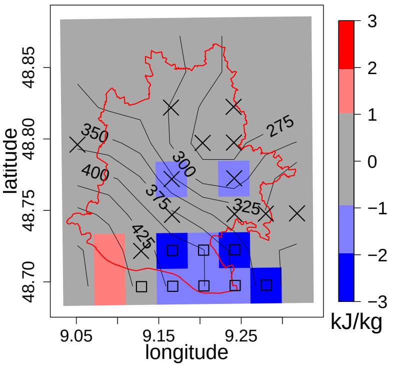

Figure 6.30: Same as Fig. 6.25, but for mean summer sum of CAPE

6.6.5 Summary Green Scenario Projection

For the green scenario, a slight decrease in mean summer 2 m temperature occurs at several grid points that were reforested or covered by urban land use. But for most of these grid cells, the decrease is not larger than 0.1 K. The mean number of frost days decreases at several grid points, especially at reforested grid cells. Precipitation changes hardly for the green scenario as well, the mean summer sum decreases at several grid points by approximately 15 mm, but the mean number of days with extreme precipitation changes by no more than one day. Only at reforested grid points, the amount of global radiation decreases by small amounts of up to 17 kWh/m^2. Also for mean summer specific humidity, the only changes develop above reforested grid points where humidity decreases by up to 0.15 g/kg. The mean summer sum of CAPE decreases here as well, but also at the two grid points with the largest absolute difference of Q_F.

The mitigation measures of the urban grid points cause only a small decrease in temperature, precipitation and CAPE, reforestation however leads to slightly larger decreases in temperature, global radiation, specific humidity and CAPE at these grid points. Still, all changes caused by the green scenario are small and mostly restricted to grid points with alternated land use. They are not able to diminish the differences caused by climate change in the SMA. As for the red scenario, ensemble simulations would help assessing the spread of changes caused by land use modifications.

6.7 Quantification of the Impacts of Climate Change and Land Use Change for the City Centre

To decide whether climate change or urban land use change has a larger impact on the urban climate in the city centre of Stuttgart, Tab. 6.1 contrasts the differences caused by climate change on the one hand and by the two land use scenarios on the other hand. The table consists of the mean changes of the variables discussed above, averaged over the grid points as indicated in Fig. 6.31 by the black frame. This is a relevant area, as it is frequented by many people during daytime. One of the four grid points belongs to LCZ 2 for both the reference and the red scenario land use, another one is assigned LCZ 5 for the reference land use and changes to LCZ 2 in the red scenario as well. The two forest grid points change to LCZ 2 and 6 in the red scenario. So this smaller domain represents urbanisation quite well, but still the grid box with an anthropogenic heat input of 300 W/m^2 for the red scenario is not directly involved in the final analysis. It was interesting to see what effects such an extreme addition of Q_F can cause (e. g., the evolving urban breeze), but for a more realistic analysis, this grid point is excluded. Also, the chosen grid points are not influenced by the land use change from agriculture to mixed forest in the green scenario.

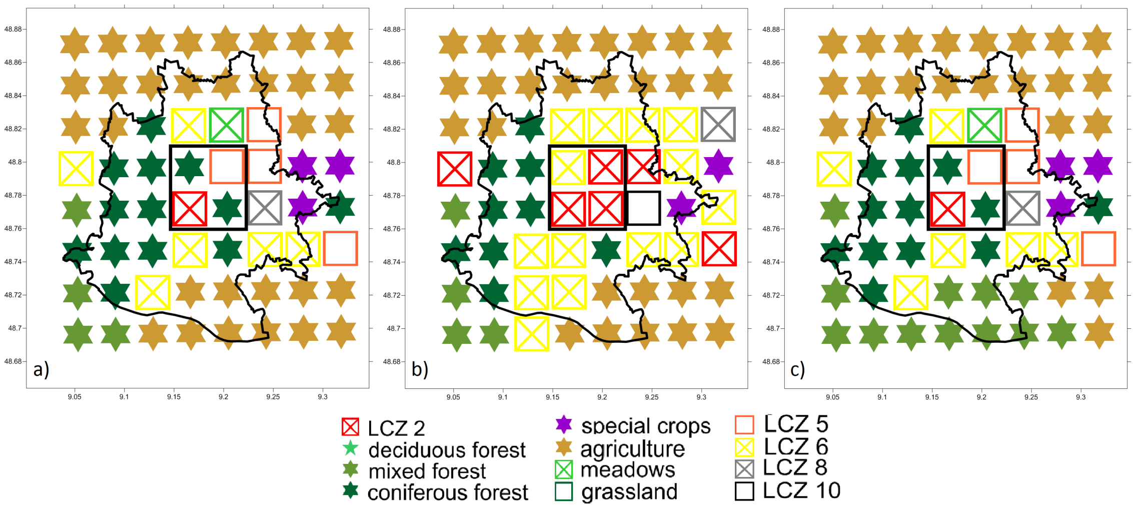

Figure 6.31: Land use distribution of (a) control run and reference projection, (b) red scenario projection, (c) green scenario projection on 2.8 km-grid with city centre indicated by the black frame.

The mean summer 2 m temperature increases significantly by 0.87 K through climate change (Tab. 6.1). For the red scenario, additional 0.15 K add up to a total increase of 1.02 K, in the green scenario, temperature decreases by 0.06 K compared to the reference projection.

The mean number of summer days increases by 5.3 from the control run to the reference projection. Additional 0.8 days are added for the red scenario, and 0.2 are subtracted for the green scenario. So for summer mean temperature and the mean number of summer days, climate change is responsible for the major impact.

When looking at the mean number of frost days, however, the differences caused by the change in land use (-1.9 days and +1.6 days for red and green scenario respectively) amount to nearly the same order of magnitude as that caused by climate change (+2.7 days). Nevertheless, the relative changes are not very large.

The mean summer precipitation of the reference projection is 42 mm (6.2 %) larger than that of the control simulation. It decreases for both the red scenario projection and the green scenario projection by 14 and 20 mm respectively compared to the reference projection. So land use change reduces the impact of climate change on mean summer precipitation, but again the changes are small and climate change has the larger impact on this variable as well.

Land use change has no impact on the mean number of days with extreme precipitation (20 mm or greater). Climate change, however, is responsible for additional 1.6 days of extreme precipitation on average.

The red scenario land use distribution has the largest influence on mean summer vertical wind speed, it causes an additional subsidence of 2.41 mm/s. However, one has to keep in mind that in the area analysed in this section, the easterly neighbouring grid point to

Variable	Unit	Control	Reference - control	Red scenario - reference	Green scenario - reference
2 m temperature, summer	K	286.95	0.87	0.15	-0.06
Summer days	days	4.6	5.3	0.8	-0.2
Frost days	days	32.0	2.7	-1.9	1.6
Precipitation, summer sum	mm	681	42	-14	-20
Days of extreme precipitation, summer	days	7.6	1.6	0.0	-0.3
Vertical wind speed at appr. 530 m above ground, summer	mm/s	-3.46	-1.28	-2.41	0.00
Global radiation, summer sum	kWh/m^2	696	-24	12	1
2 m specific humidity, summer	g/kg	7.730	0.026	-0.006	-0.005
CAPE, summer sum	kJ/kg	96.4	-5.1	0.6	-0.8
Total cloud cover, summer	%	77.94	1.31	0.03	-0.03

Table 6.1: Mean variables for control simulation, difference between reference projection and control simulation, and between the two scenarios and the reference projection, respectively, averaged over the city centre. Significant differences (on 95 %-level, tested on daily values where possible) are marked yellow.

the LCZ 10-grid point that has been discussed in detail in section 6.5.3 is included. At this easterly grid point, the descending branch of the urban breeze induced by the anthropogenic heat input of 300 W/m^2 is located. This probably causes most of this large difference. For the green scenario projection, no change of vertical wind occurs and climate change causes additional subsidence of 1.28 mm/s.

Global radiation decreases significantly by 24 kWh/m^2 from the control simulation to the reference simulation. For the red scenario simulation, half of this decrease is compensated with an increase by 12 kWh/m^2 when comparing the red scenario and reference projections. The green scenario has no influence on global radiation in Stuttgart's city centre.

Even though the increase in 2 m specific humidity by 0.026 g/kg due to climate change is small, it is significant when looking at its daily mean. However, both red and green scenarios hardly change humidity.

The mean summer sum of CAPE decreases through climate change by 5.1 kJ/kg. The red scenario slightly compensates this by an addition of 0.6 kJ/kg, the green scenario further decreases CAPE by 0.8 kJ/kg.

Climate change increases the mean summer total cloud cover by 1.31 percentage points, which is significant when looking at daily mean total cloud cover. Neither the red nor the green scenario have an impact on total cloud cover.

All in all, climate change has the larger impact on the mean climate of both the city centre of Stuttgart and the entire SMA. The spatial analysis of the mean changes in summer variables showed several interesting features, like the triggering of an urban breeze above the LCZ 10-grid point, and allowed some general conclusions on the impact of land use on several variables.

7. Summary and Outlook

Summary

The objective of this thesis was to analyse the combined impacts of urbanisation and climate change on the climate of the Stuttgart Metropolitan Area (SMA). This was done by conducting coupled high-resolution climate simulations with COSMO-CLM and Veg3D. For a better representation of urban climate, additional urban land use classes were added to Veg3D and anthropogenic heat input was incorporated.

The simulations were conducted for a control period (1971-1975) and a projection period (2021-2025). To study the range of possible effects of urban development on future urban climate, two contrasting scenarios for the projection period were developed. The green scenario implies less energy consumption and an increase in vegetated surfaces in urban areas as well as reforestation of an agricultural area in the south of Stuttgart, the red scenario assumes an enlargement and densification of built-up areas. An additional projection simulation with the current land use distribution was done in order to separate the respective effects of climate change and land use change.

First, stand-alone simulations were conducted to test the successful implementation of the applied modifications of Veg3D. As expected, they resulted in an increase in average soil temperature. Additionally, these simulations showed that after one year of simulation time, temperature increase had not converged on a constant value in the lower layers. Thus, for the control run, a cyclical spin-up of four years for the soil was applied.

The effects of the green and red scenario were tested in stand-alone mode as well. The green scenario caused an average soil temperature decrease by about 2.5 K, the red scenario resulted in a soil temperature increase by about 1 K compared to the reference situation.

In the city centre of Stuttgart, the coupled simulations resulted in a significant increase in 2 m summer temperature by 0.87 K through climate change in the analysed time periods. The effects of the two scenarios were smaller with an increase by 0.15 K caused by the red scenario and a decrease by 0.06 K by the green scenario, compared to the reference projection. Small but significant changes through climate change also evolved for global radiation, specific humidity and total cloud cover. The changes of these variables caused by the two land use scenarios were considerably smaller in the city centre.

When looking at the entire SMA, at some grid points that were subject to modifications in land use, differences to the reference projection were in the order of magnitude of the changes caused by climate change. But as the climate change signal at these grid boxes was already small, the relevance of the changes caused by modified land use is reduced. One grid point in the red scenario was assigned LCZ 10 with the high amount of 300 W/m^2 as anthropogenic heat input. At this grid point, temperature increased significantly and a small cell of local convection developed.

The answer to the introductory question of the respective impacts of climate change and land use change on the local climate of the SMA is that climate change has a considerably larger influence on local climate for the periods considered in this thesis.

Outlook

The simulations that have been conducted for this thesis should be continued to obtain longer time periods. Thus, the analysis would allow more robust conclusions both on the effects of climate change and land use change. It is also possible that on longer time scales, the influence of changed grid points on their surrounding will appear more clearly.

Additional types of analysis could be conducted with simulation results of longer time periods. The effects of climate change and land use change on extreme events could be evaluated, for example by calculating return values of extreme precipitation events or examining the duration of heat waves.

Stuttgart's *Kessellage* favours the formation of low-level temperature inversions leading to bad air quality. Thus, it would be interesting to analyse the impacts of climate change and land use change on the frequency of occurrence and the vertical extent of inversions. Especially the high amount of anthropogenic heat of 300 W/m^2 might prevent the atmosphere from stabilising. Atmospheric stability could be assessed from calculating a vertical gradient of potential temperature.

The impact of climate and land use changes on humans could be studied more specifically. The 'Klima-Michel-model' (Jendritzky et al., 2001), for example, provides a method of assessing human comfort from Synop observations (2 m temperature and dew point temperature, wind velocity, cloud amounts and cloud types in all levels). This approach could also be applied to the output of a climate model.

Various changes do evolve for the two land use scenarios, but most of them are so small that they could probably not be detected in observations. An ensemble of simulations would help to assess the possible spread of differences caused by land use modifications.

Simulations of higher resolution, for example at a horizontal grid spacing of 1 km, would add accuracy to the distribution of land use classes, the resolution of the topography and the atmospheric model in general. Also, the impacts of the modified land use parametrisation and land use scenarios could be analysed in more detail. An intermediate step of higher resolution could also be applied, the so called 'tile-approach'. This means that the SVAT-model is run on a higher resolution than the atmospheric model. Thus, at least a more detailed land use distribution would be incorporated.

So far, soil layers do not interact horizontally in Veg3D. Because of this, grid points with anthropogenic heat input Q_F > 0 influence neighbouring grid points only through the atmospheric model. But as Q_F is implemented in the soil energy balance, interaction in the soil should be incorporated as well.

The cyclical spin-up of Veg3D could also be improved. So far, it is not truly periodical as simply the coupled model output of one year is used as forcing. Thus, an unreasonable break can occur after December 31st when the fields of January 1st are applied. A smooth transition between the turn of the year should be implemented.

Additional validations of the applied parametrisation of urban areas are necessary. Thus, the parameters of the land use classes could be adjusted. For example, $Q_F =$ 300 W/m^2 of LCZ 10 could be lowered to a more reasonable value. Moreover, an annual or daily cycle of Q_F could be implemented to parametrise it more accurately. For instance, the values mentioned in section 2.2 of 15 W/m^2 for summer and 70 W/m^2 for winter given by Pigeon et al. (2007) could be used as minimum and maximum for an annual cycle of LCZ 2.

After additional verification of the parametrisation of urban areas presented in this thesis, the method should also be applied on other cities.

Bibliography

Adachi, S. A., F. Kimura, H. Kusaka, T. Inoue, and H. Ueda, 2012: Comparison of the impact of global climate changes and urbanization on summertime future climate in the tokyo metropolitan area. *J. Appl. Meteor. Climatol.*, **51 (8)**, 1441–1454.

Adrian, G. and D. Frühwald, 2002: Design der neuen Modellkette GME/LM. *promet*, **27**, 106–110.

Amt für Umweltschutz Stuttgart, 2013: Historie der Stadtklimatologie. Accessed on 2014/01/27, `http://www.stadtklima-stuttgart.de/index.php?service_kontakt_75_jahre_stadtklimatologie`.

Bartholomé, E. and A. S. Belward, 2005: GLC2000: a new approach to global land cover mapping from Earth observation data. *Int. J. Remote Sens.*, **26 (9)**, 1959–1977.

Best, M., 1998: Representing urban areas in numerical weather prediction models. *Proc. Second Urban Environment Symp*.

Best, M., 2006: Progress towards better weather forecasts for city dwellers: from short range to climate change. *Theor. Appl. Climatol.*, **84 (1-3)**, 47–55.

Braun, F. J., 2002: Mesoskalige Modellierung der Bodenhydrologie. Ph.D. thesis, Universität Karlsruhe.

Carlson, T., J. Dodd, S. Benjamin, and J. Cooper, 1981: Satellite Estimation of the Surface Energy Balance, Moisture Availability and Thermal Inertia. *J. Appl. Meteor.*, **20**, 67–87.

Doms, G., 2011: A Description of the Nonhydrostatic regional COSMO-Model - Part 1: Dynamics and Numerics. `www.cosmo-model.org`.

Evans, J. M. and S. de Schiller, 1996: Application of microclimate studies in town planning: A new capital city, an existing urban district and urban river front development. *Atmos. Environ.*, **30**, 361–364.

Fosser, G., 2013: Precipitation statistics from regional climate model at resolutions relevant for soil erosion. Ph.D. thesis, Karlsruher Institut für Technologie.

Früh, B., M. Koßmann, and M. Roos, 2011: Frankfurt am Main im Klimawandel - Eine Untersuchung zur städtischen Wärmebelastung. *Ber. Dtsch. Wetterd.*, **237**.

Grothues, E., et al., 2012: Klimawandelgerechte Metropole Köln - Abschlussbericht. *Fachbericht 50. Online at: http://www.lanuv.nrw.de/veroeffentlichungen/ fachberichte/fabe50/fabe50start.htm (accessed on 2014/08/21)*.

Hackenbruch, J., 2015: Personal communication. January 2015.

Hamdi, R., H. Van De Vyver, R. De Troch, and P. Termonia, 2013: Assessment of three dynamical urban climate downscaling methods: Brussels's future urban heat island under an A1B emission scenario. *Int. J. Climatol.*, **34**, 978–999.

Hidalgo, J., V. Masson, A. Baklanov, G. Pigeon, and L. Gimeno, 2008a: Advances in Urban Climate Modeling. *Ann. N. Y. Acad. Sci.*, **1146**, 354–374.

Hidalgo, J., V. Masson, and L. Gimeno, 2010: Scaling the daytime urban heat island and urban-breeze circulation. *J. Appl. Meteor. Climatol.*, **49 (5)**, 889–901.

Hidalgo, J., G. Pigeon, and V. Masson, 2008b: Urban-breeze circulation during the CAPITOUL experiment: observational data analysis approach. *Meteorol. Atmos. Phys.*, **102 (3-4)**, 223–241.

Hoffmann, K., W. Bivour, B. Früh, M. Koßmann, and P.-H. Voß, 2014: Klimauntersuchungen in Jena für die Anpassung an den Klimawandel und seine erwarteten Folgen. *Ber. Dtsch. Wetterd.*, **243**.

Hoffmann, P., O. Krueger, and K. H. Schlünzen, 2012: A statistical model for the urban heat island and its application to a climate change scenario. *Int. J. Climatol.*, **32 (8)**, 1238–1248.

Jendritzky, G., A. Maarouf, and H. Staiger, 2001: Looking for a Universal Thermal Climate Index UTCI for outdoor applications. *Windsor-Conference on Thermal Standards*, 5–8.

KLIWA, 2013: Klimaveränderung und Konsequenzen für die Wasserwirtschaft. KLIWA-Berichte.

Knote, C., G. Heinemann, and B. Rockel, 2010: Changes in weather extremes: Assessment of return values using high resolution climate simulations at convection-resolving scale. *Meteor. Z.*, **19 (1)**, 11–23.

Kohlhepp, R., 2009: Berücksichtigung der anthropogenen Wärmefreisetzung in COSMO-CLM. M.S. thesis, Universität Karlsruhe, Germany.

Kusaka, H., M. Hara, and Y. Takane, 2012: Urban climate projection by the WRF model at 3-km horizontal grid increment: dynamical downscaling and predicting heat stress in the 2070's August for Tokyo, Osaka, and Nagoya metropolises. *J. Meteor. Soc. Japan*, **90 (0)**, 47–63.

Landeshauptstadt Stuttgart, 2008: Klimaatlas Region Stuttgart. *Schr.reihe Verband Region Stuttgart*, **26**.

Landeshauptstadt Stuttgart, 2010: Der Klimawandel - Herausforderungen für die Stadtklimatologie.

Martilli, A., A. Clappier, and M. W. Rotach, 2002: An urban surface exchange parameterisation for mesoscale models. *Bound.-Lay. Metetorol.*, **104 (2)**, 261–304.

McCarthy, M. P., M. J. Best, and R. A. Betts, 2010: Climate change in cities due to global warming and urban effects. *Geophys. Res. Lett.*, **37 (9)**.

Meißner, C., 2008: High-resolution sensitivity studies with the regional climate model COSMO-CLM. Ph.D. thesis, Universität Karlsruhe.

Moss, R. H., et al., 2010: The next generation of scenarios for climate change research and assessment. *Nature*, **463 (7282)**, 747–756.

Nachtergaele, F., et al., 2008: Harmonized World Soil Database. *FAO*.

Nationalatlas, 2003: Nationalatlas Bundesrepublik Deutschland, Band 3, Klima Pflanzen und Tierwelt.

Oke, T., 1982: The energetic basis of the urban heat island. *Quart. J. Roy. Meteor. Soc.*, **108 (455)**, 1–24.

Oke, T. R., 1984: Towards a Prescription for the Greater Use of Climatic Principles in Settlement Planning. *Energy Build.*, **7**, 1–10.

Oke, T. R., 1993: *Boundary layer climates*. 2d ed., Routledge, London [u.a.].

Pigeon, G., D. Legain, P. Durand, and V. Masson, 2007: Anthropogenic heat release in an old European agglomeration (Toulouse, France). *Int. J. Climatol.*, **27**, 1969–1981.

Rauthe, M., H. Steiner, U. Riediger, A. Mazurkiewicz, and A. Gratzki, 2000: A Central European precipitation climatology–Part I: Generation and validation of a high-resolution gridded daily data set (HYRAS). *Meteor. Z.*, **1 (1)**, 1–23.

Rizwan, A. M., Y. C. L. Dennis, and C. Liu, 2008: A review on the generation, determination and mitigation of Urban Heat Island. *J. Environ. Sci.*, **20**, 120–128.

Rummukainen, M., 2010: State-of-the-art with regional climate models. *Wiley Interdisciplinary Reviews: Climate Change*, **1 (1)**, 82–96.

Sailor, D. J., 1995: Simulated urban climate response to modifications in surface albedo and vegetative cover. *J. Appl. Meteor.*, **34 (7)**, 1694–1704.

Schädler, G., 1990: Numerische Simulationen zur Wechselwirkung zwischen Landoberflächen und atmosphärischer Grenzschicht. Ph.D. thesis, Universität Karlsruhe.

Scheef, R., 1976: Stadtentwicklung und Stadtklima: Stuttgart, ein Beispiel aus der Bundesrepublik Deutschland. Part of German contribution to UN Habitat 1976 conference, Farbfilm.

Schoetter, R., D. Grawe, P. Hoffmann, P. Kirschner, A. Grätz, and K. H. Schlünzen, 2013: Impact of local adaptation measures and regional climate change on perceived temperature. *Meteor. Z.*, **22 (2)**, 117–130.

Stewart, I. and T. Oke, 2012: Local Climate Zones for Urban Temperature Studies. *Bull. Amer. Meteor. Soc.*, **93**, 1879–1900.

Stewart, I., T. Oke, and E. Krayenhoff, 2014: Evaluation of the 'local climate zone' scheme using temperature observations and model simulations. *Int. J. Climatol.*, **34**, 1062–1080.

Taha, H., 1997: Urban climates and heat islands: albedo, evapotranspiration, and anthropogenic heat. *Energy Build.*, **25**, 99–103.

Wilby, R. L., 2008: Constructing climate change scenarios of urban heat island intensity and air quality. *Environ. Plan. B - Plan. Des.*, **35 (5)**, 902.

List of Figures

List of Tables

A. Appendix

A.1 List of Abbreviations

BEP	Building Effect Parametrisation
CAPE	Convective Available Potential Energy
COSMO	COnsortium for Small-scale MOdelling
COSMO-CLM	COSMO in CLimate Mode
DWD	Deutscher WetterDienst (German weather service)
ECHAM6	ECMWF HAMburg GCM, version 6
ECMWF	European Centre for Medium-range Weather Forecast
ERA40	ECMWF Re-Analysis (40 years)
GCM	General Circulation Model
GLC2000	Global Land Cover 2000
HLRS	HöchstLeistungsRechenzentrum Stuttgart (High Performance Computing Center Stuttgart)
HWSD	Harmonized World Soil Database
IC2	InstitutsCluster 2
KIT	Karlsruher Institut für Technologie (Karlsruhe Institute of Technology)
LAI	Leaf Area Index
LCZ	Local Climate Zone
MUKLIMO	Mikroskaliges Urbanes KLImaMOdell (microscale urban climate model)
NWP	Numerical Weather Prediction
RCM	Regional Climate Model
RCP	Representative Concentration Pathways
RMSE	Root Mean Square Error

SMA	Stuttgart Metropolitan Area
SPOT	Satellite Pour l'Observation de la Terre (Satellite for observation of Earth)
SVAT	Soil-Vegetation-Atmosphere-Transfer
UHI	Urban Heat Island

Table A.1: Abbreviations used in this thesis

A.2 Additional Figures of Chapter 6

Section 6.4

Fig. A.1

Section 6.5

Fig. A.2, A.3, A.4, A.5, A.6, A.7, A.8, A.9, A.10, A.11

Section 6.6

Fig. A.12, A.14, A.15, A.16, A.17,A.18, A.19, A.20, A.21

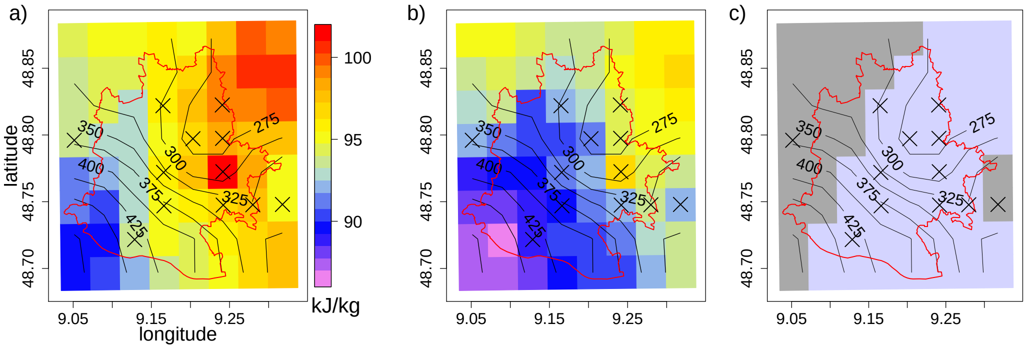

Figure A.1: Mean summer sum of CAPE of first five analysis years, (a) control run 1971-1975, (b) reference projection 2021-2025, (c) difference between projection and control run. Circles mark significant differences on a 95 %-level, crosses indicate urban land use, black lines show the height of the terrain and the area of Stuttgart is indicated by the red polygon.

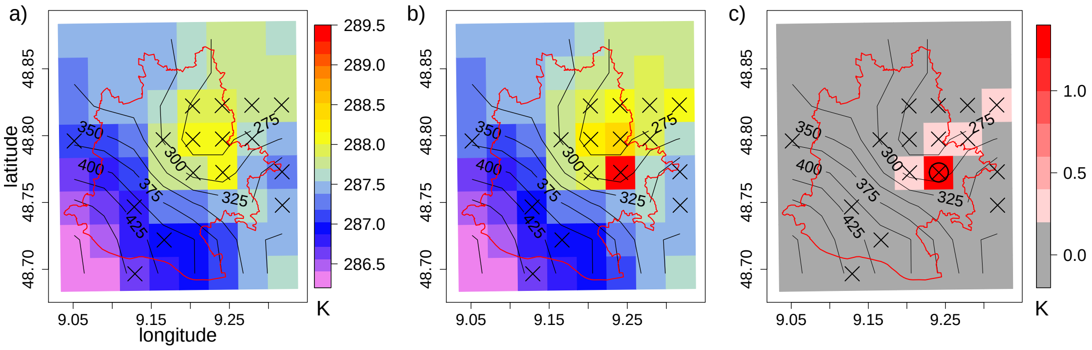

Figure A.2: Mean summer 2 m temperature 2021-2025, (a) reference projection, (b) red scenario projection, (c) difference between red scenario and reference projection. Circles mark significant differences on a 95 %-level, crosses indicate intensified grid points, black lines show the height of the terrain and the area of Stuttgart is indicated by the red polygon.

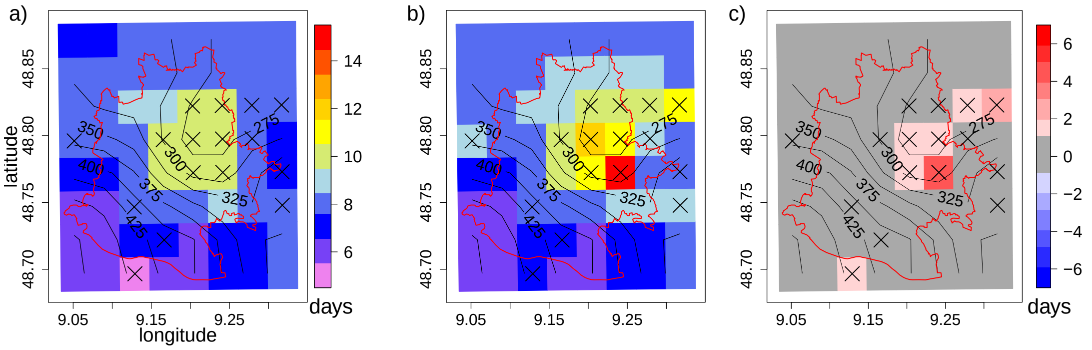

Figure A.3: Mean annual number of summer days ($T_{max} \geq 25\,^{\circ}$ C) 2021-2025, (a) reference projection, (b) red scenario projection, (c) difference between red scenario and reference projection. Circles mark significant differences on a 95 %-level, crosses indicate intensified grid points, black lines show the height of the terrain and the area of Stuttgart is indicated by the red polygon.

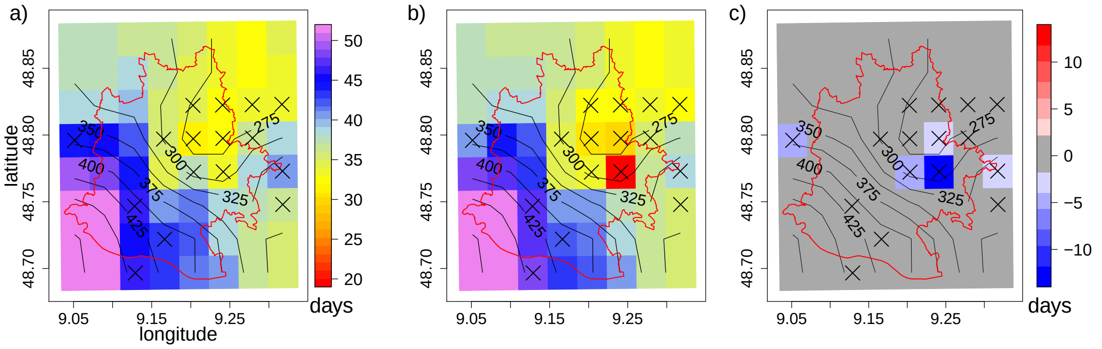

Figure A.4: Mean annual number of frost days ($T_{min} < 0\,^{\circ}$ C) 2021-2025, (a) reference projection, (b) red scenario projection, (c) difference between red scenario and reference projection. Circles mark significant differences on a 95 %-level, crosses indicate intensified grid points, black lines show the height of the terrain and the area of Stuttgart is indicated by the red polygon.

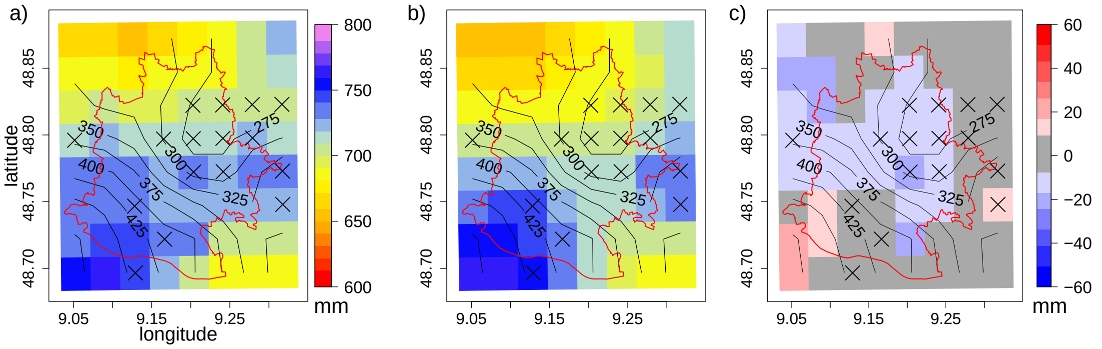

Figure A.5: Mean summer precipitation sum 2021-2025, (a) reference projection, (b) red scenario projection, (c) difference between red scenario and reference projection. Circles mark significant differences on a 95 %-level, crosses indicate intensified grid points, black lines show the height of the terrain and the area of Stuttgart is indicated by the red polygon.

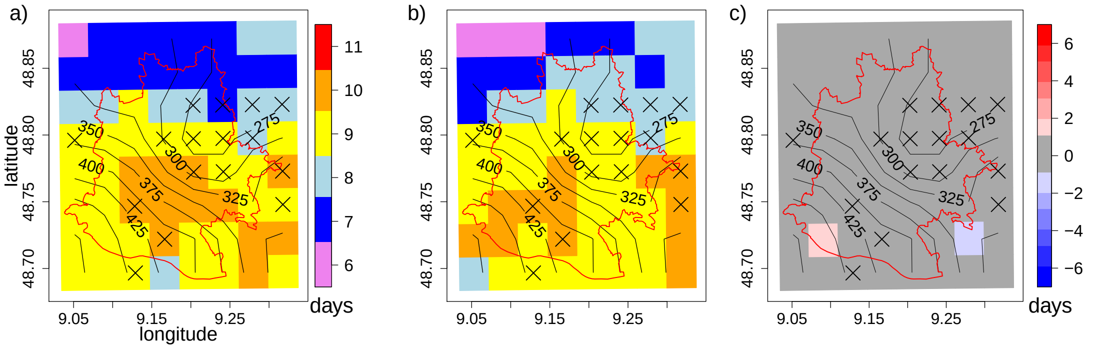

Figure A.6: Mean annual number of summer daily sum of precipitation $\geq$ 20 mm 2021-2025, (a) reference projection, (b) red scenario projection, (c) difference between red scenario and reference projection. Circles mark significant differences on a 95 %-level, crosses indicate intensified grid points, black lines show the height of the terrain and the area of Stuttgart is indicated by the red polygon.

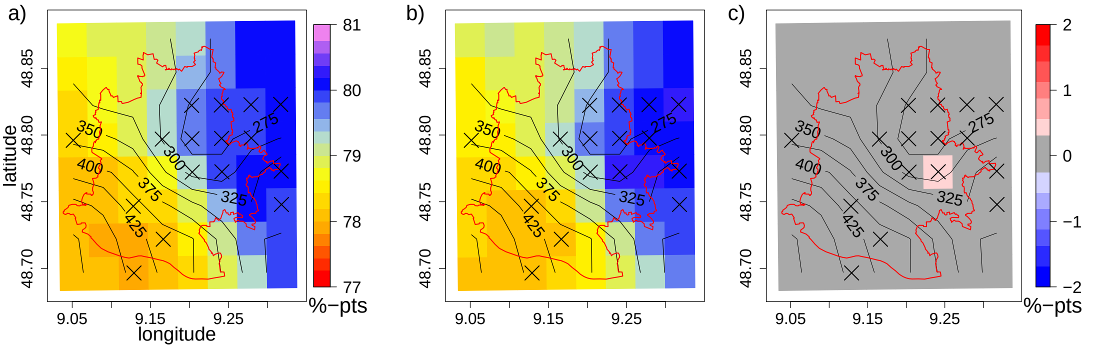

Figure A.7: Mean summer total cloud cover 2021-2025, (a) reference projection, (b) red scenario projection, (c) difference between red scenario and reference projection. Circles mark significant differences on a 95 %-level, crosses indicate intensified grid points, black lines show the height of the terrain and the area of Stuttgart is indicated by the red polygon.

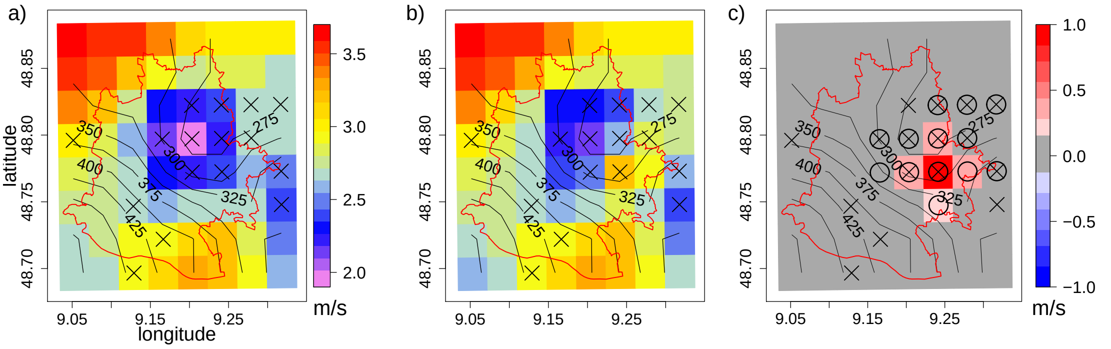

Figure A.8: Mean summer amount of 10 m horizontal wind during the day (8:00-19:00) 2021-2025, (a) reference projection, (b) red scenario projection, (c) difference between red scenario and reference projection. Circles mark significant differences on a 95 %-level, crosses indicate intensified grid points, black lines show the height of the terrain and the area of Stuttgart is indicated by the red polygon.

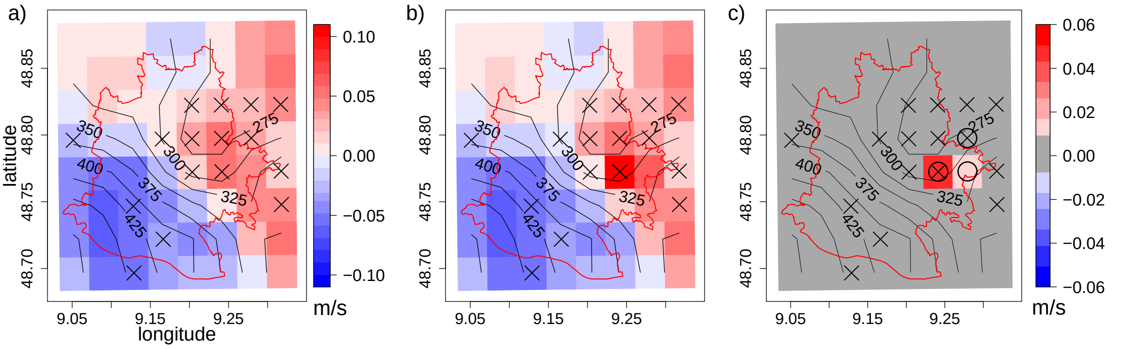

Figure A.9: Mean vertical wind speed during summer at appr. 540 m during the night (20:00 - 7:00) 2021-2025, (a) reference projection, (b) red scenario projection, (c) difference between red scenario and reference projection. Circles mark significant differences on a 95 %-level, crosses indicate intensified grid points, black lines show the height of the terrain and the area of Stuttgart is indicated by the red polygon.

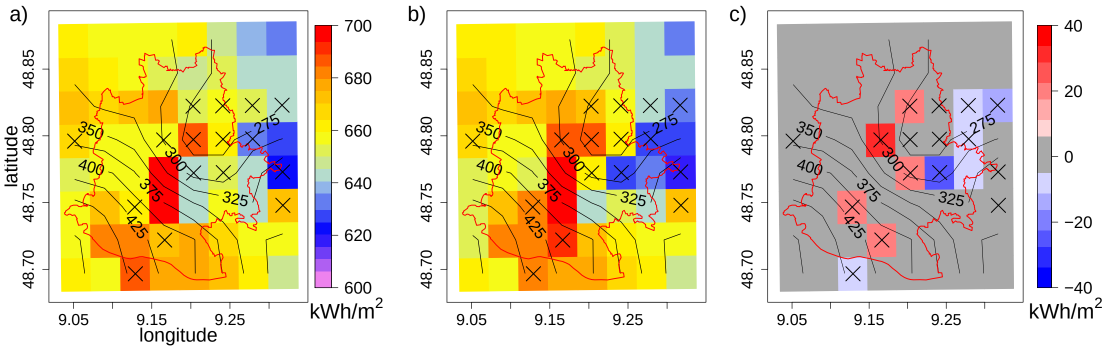

Figure A.10: Mean summer sum of global radiation 2021-2025, (a) reference projection, (b) red scenario projection, (c) difference between red scenario and reference projection. Circles mark significant differences on a 95 %-level, crosses indicate intensified grid points, black lines show the height of the terrain and the area of Stuttgart is indicated by the red polygon.

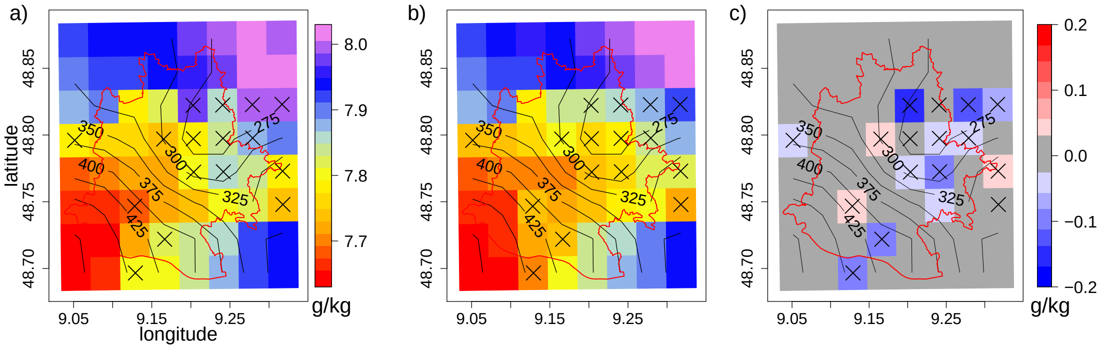

Figure A.11: Mean summer 2 m specific humidity 2021-2025, (a) reference projection, (b) red scenario projection, (c) difference between red scenario and reference projection. Circles mark significant differences on a 95 %-level, crosses indicate intensified grid points, black lines show the height of the terrain and the area of Stuttgart is indicated by the red polygon.

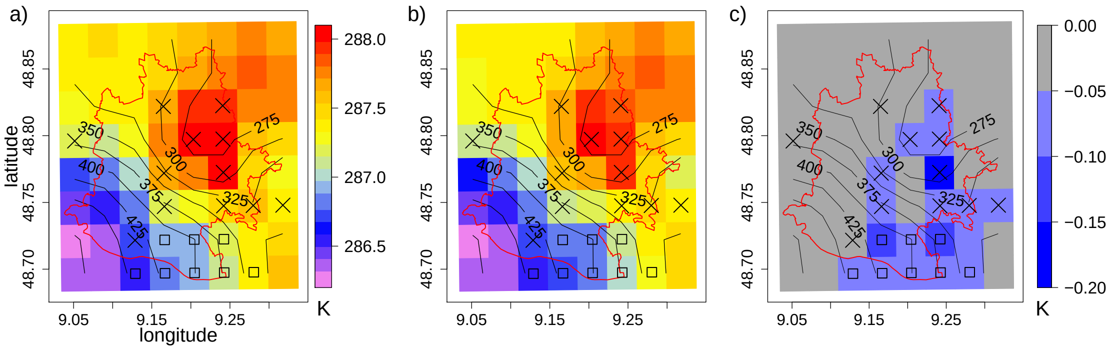

Figure A.12: Mean summer 2 m temperature 2021-2025, (a) reference projection, (b) green scenario projection, (c) difference between green scenario and reference projection. Circles would mark significant differences on a 95 %-level, crosses indicate urban land use, squares indicate reforestation, black lines show the height of the terrain and the area of Stuttgart is indicated by the red polygon.

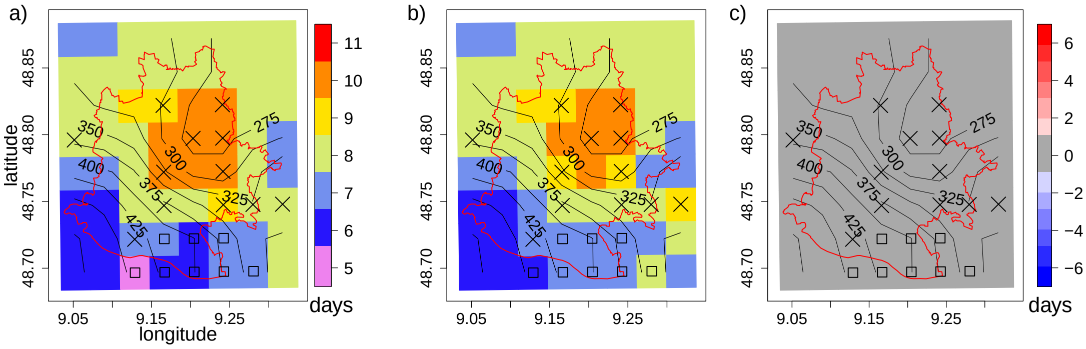

Figure A.13: Mean annual number of summer days ($T_{max} \geq 25\,^\circ$ C) 2021-2025, (a) reference projection, (b) green scenario projection, (c) difference between green scenario and reference projection. Circles would mark significant differences on a 95 %-level, crosses indicate urban land use, squares indicate reforestation, black lines show the height of the terrain and the area of Stuttgart is indicated by the red polygon.

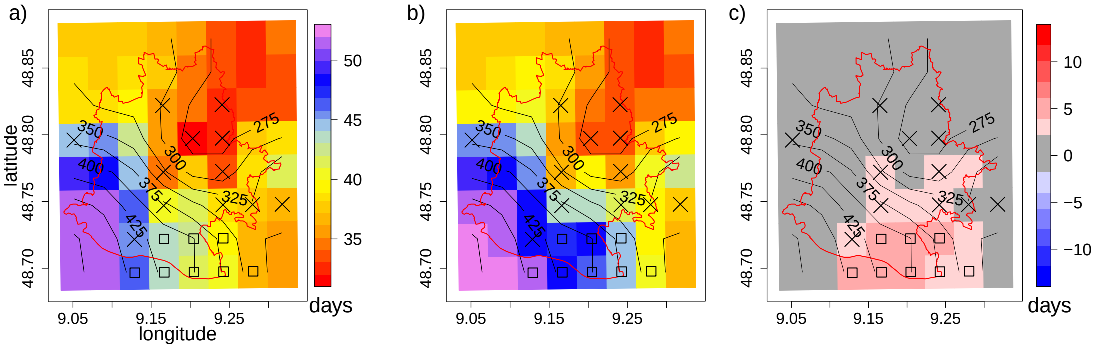

Figure A.14: Mean annual number of frost days ($T_{min} < 0\,^\circ$ C) 2021-2025, (a) reference projection, (b) green scenario projection, (c) difference between green scenario and reference projection. Circles would mark significant differences on a 95 %-level, crosses indicate urban land use, squares indicate reforestation, black lines show the height of the terrain and the area of Stuttgart is indicated by the red polygon.

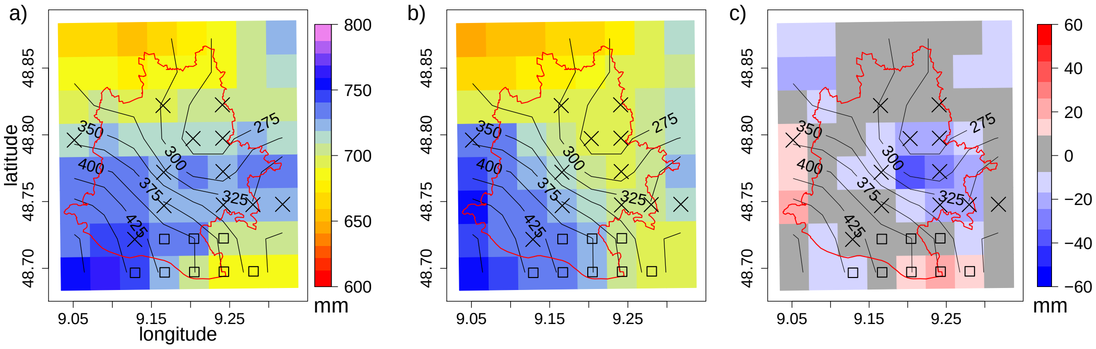

Figure A.15: Mean summer precipitation sum 2021-2025, (a) reference projection, (b) green scenario projection, (c) difference between green scenario and reference projection. Circles would mark significant differences on a 95 %-level, crosses indicate urban land use, squares indicate reforestation, black lines show the height of the terrain and the area of Stuttgart is indicated by the red polygon.

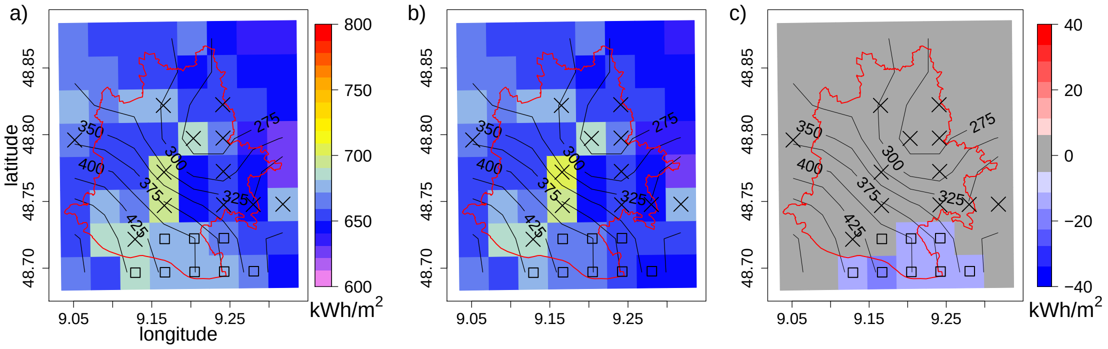

Figure A.16: Mean summer sum of global radiation 2021-2025, (a) reference projection, (b) green scenario projection, (c) difference between green scenario and reference projection. Circles would mark significant differences on a 95 %-level, crosses indicate urban land use, squares indicate reforestation, black lines show the height of the terrain and the area of Stuttgart is indicated by the red polygon.

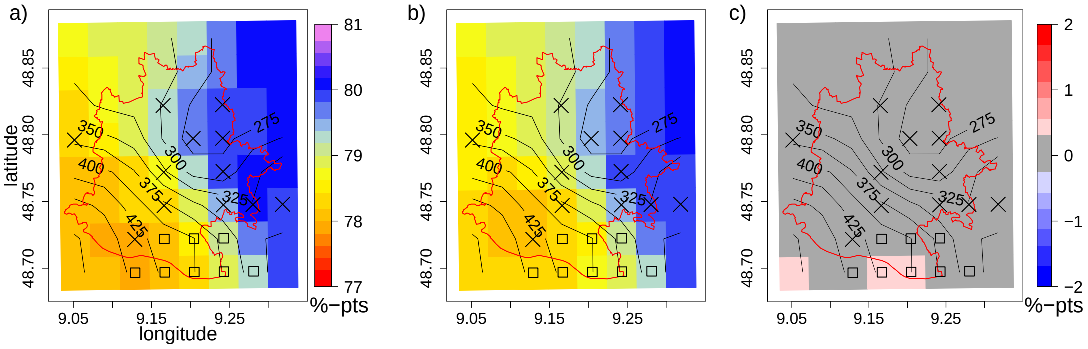

Figure A.17: Mean summer total cloud cover 2021-2025, (a) reference projection, (b) green scenario projection, (c) difference between green scenario and reference projection. Circles would mark significant differences on a 95 %-level, crosses indicate urban land use, squares indicate reforestation, black lines show the height of the terrain and the area of Stuttgart is indicated by the red polygon.

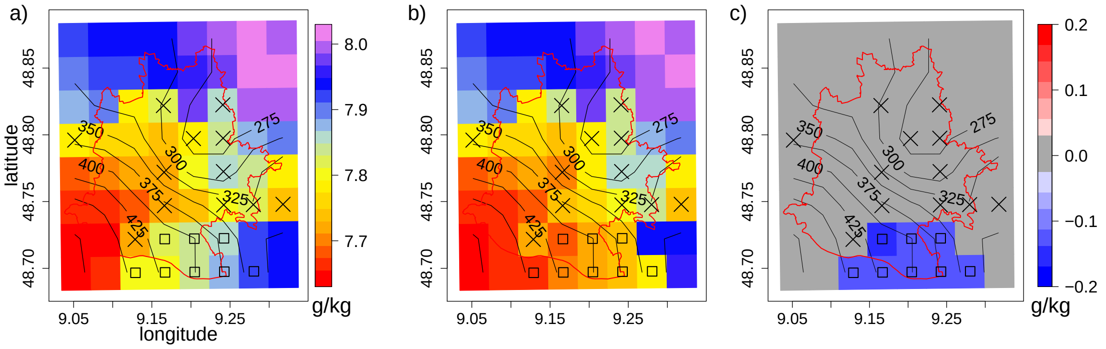

Figure A.18: Mean summer 2 m specific humidity 2021-2025, (a) reference projection, (b) green scenario projection, (c) difference between green scenario and reference projection. Circles would mark significant differences on a 95 %-level, crosses indicate urban land use, squares indicate reforestation, black lines show the height of the terrain and the area of Stuttgart is indicated by the red polygon.

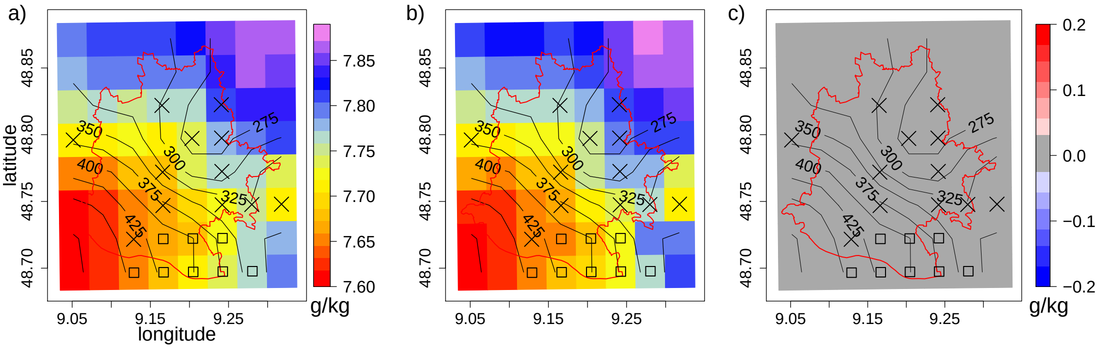

Figure A.19: Mean summer specific humidity in the lowest appr. 20 m of the atmosphere 2021-2025, (a) reference projection, (b) green scenario projection, (c) difference between green scenario and reference projection. Circles would mark significant differences on a 95 %-level, crosses indicate urban land use, squares indicate reforestation, black lines show the height of the terrain and the area of Stuttgart is indicated by the red polygon.

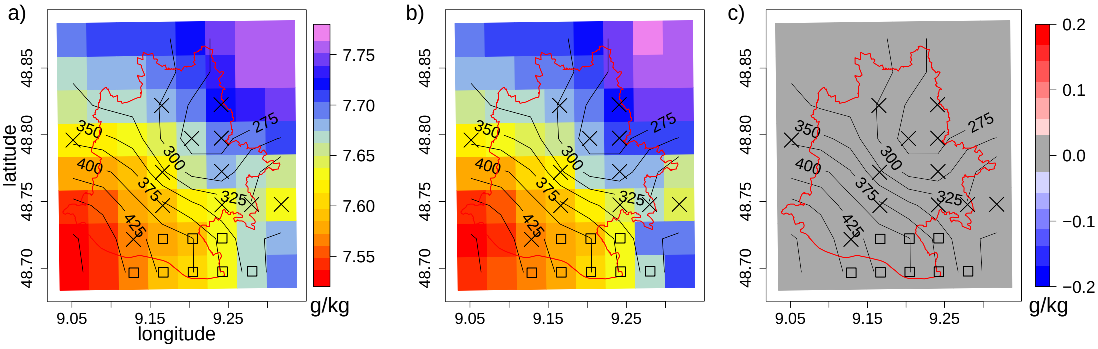

Figure A.20: Mean summer specific humidity between appr. 20 and 50 m above ground 2021-2025, (a) reference projection, (b) green scenario projection, (c) difference between green scenario and reference projection. Circles would mark significant differences on a 95 %-level, crosses indicate urban land use, squares indicate reforestation, black lines show the height of the terrain and the area of Stuttgart is indicated by the red polygon.

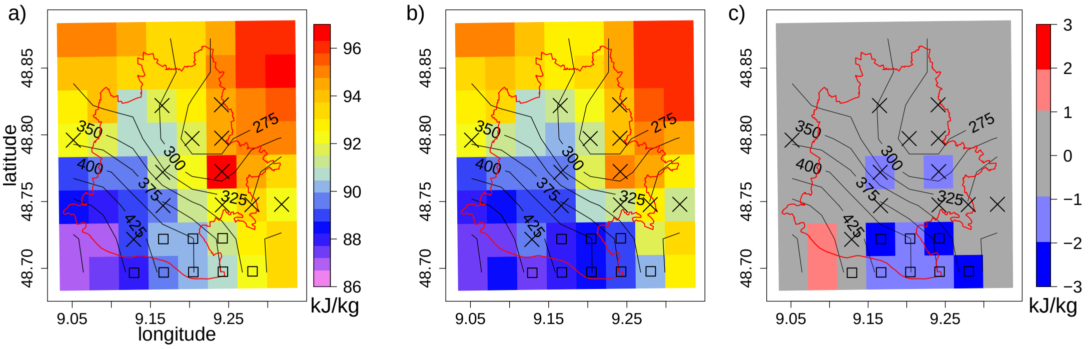

Figure A.21: Mean summer sum of CAPE 2021-2025, (a) reference projection, (b) green scenario projection, (c) difference between green scenario and reference projection. Circles would mark significant differences on a 95 %-level, crosses indicate urban land use, squares indicate reforestation, black lines show the height of the terrain and the area of Stuttgart is indicated by the red polygon.

Danksagung

Zuallererst möchte ich Prof. Kottmeier für die Übernahme des Referats, sowie ein erstes Korrekturlesen und Anregungen zu dieser Arbeit danken. Auch Prof. Hoose danke ich für die Übernahme des Korreferats.

Besonderer Dank gilt meinem Betreuer Dr. Schädler für den Vorschlag dieser Arbeit, sowie die zahlreichen Diskussionen, Erklärungen und Anregungen vor allem in der Schlussphase der Arbeit. Und letztlich auch für das Korrekturlesen dieser schriftlichen Ausarbeitung.

Natalie Laube, die viele meiner Modellierungsprobleme teilt(e), hat mir sehr bei der Durchführung der Simulationen und auch dem Verständis der Modelle geholfen. Vielen Dank dafür! Auch mein Büronachbar Marcus Breil hat zu meinem Verständnis beigetragen und stand mir oft mit Ratschlägen zur Seite. Danke für die schöne Zeit!

Katrin Sedlmeier danke ich für die Antriebsdaten meiner Simulationen, sowie diverse Skripte und Anregungen. Ebenso danke ich den weiteren Mitgliedern der Arbeitsgruppe Julia Hackenbruch, Hans Schipper, Marianne Uhlig, Sebastian Mieruch, Hendrik Feldmann, Hans-Jürgen Panitz und Kai-Uwe Nerding für Plots, Skripte, Erklärungen und die gute Atmosphäre.

Dem Umweltamt Stuttgart danke ich für die Überlassung der Landnutzungsdaten.

Meinen Kommilitonen und Freunden sowohl in München als auch in Karlsruhe möchte ich für die Unterstützung und die schöne Studienzeit danken. Besonderer Dank geht an Julia Kosch, Vanessa Rieger und Andi Scharfstein für das Lesen der Arbeit.

Zuletzt möchte ich meiner Familie für die Unterstützung während meines gesamten Studiums danken. Besonders meinem Vater für das Korrekturlesen und Diskutieren in der Endphase dieser Arbeit.

Erklärung

Hiermit erkläre ich, dass ich die vorliegende Arbeit selbst verfasst und nur die angegebenen Hilfsmittel verwendet habe.

Ich bin damit einverstanden, dass diese Arbeit in Bibliotheken eingestellt wird und vervielfältigt werden darf.

Karlsruhe, den 21. Januar 2015

Hannah Imhof